

A STUDY OF THE FERMI SURFACE OF MERCURY

A STUDY OF THE FERMI SURFACE  
OF MERCURY USING CYCLOTRON  
RESONANCE AND MAGNETORESISTANCE

By

ARTHUR EDWARD DIXON, B.Sc., M.Sc.

A Thesis

Submitted to the Faculty of Graduate Studies

in Partial Fulfilment of the Requirements

for the Degree

Doctor of Philosophy

McMaster University

November 1966

DOCTOR OF PHILOSOPHY (1966)  
(Physics)

McMaster University  
Hamilton, Ontario.

TITLE: A Study of the Fermi Surface of Mercury using Cyclotron  
Resonance and Magnetoresistance

AUTHOR: Arthur Edward Dixon, B.Sc. (Mount Allison University)  
M.Sc. (Dalhousie University)

SUPERVISOR: Professor W. R. Datars

NUMBER OF PAGES: vii, 93

SCOPE AND CONTENTS:

A study of the Fermi surface of mercury has been carried out using cyclotron resonance and magnetoresistance techniques. Oscillations of the microwave surface impedance, which have been identified as quantum oscillations, have appeared at high magnetic field strengths, and a study of these oscillations has added more information about the Fermi surface.

The results of these experiments are compared with two models of the Fermi surface, the nearly-free-electron model, and the relativistic-augmented-plane-wave model. The relativistic-augmented-plane-wave model was found to require only small modifications to be consistent with the data.

## ACKNOWLEDGEMENTS

I am most grateful to my supervisor, Professor W. R. Datars, for his guidance and help throughout the course of this research.

The project was supported by a research grant from the National Research Council of Canada. I am also grateful to the Government of the Province of Ontario for an Ontario Graduate Fellowship.

## TABLE OF CONTENTS

	PAGE	
CHAPTER I	INTRODUCTION	1
CHAPTER II	THEORY	3
	A. Motion of an Electron in Electric and Magnetic Fields	3
	B. Cyclotron Resonance	8
	1. Physical Picture	8
	2. Azbel' - Kaner Theory	13
	C. Transverse Magnetoresistance	18
	D. Quantum Oscillations of the Microwave Surface Impedance	23
CHAPTER III	SOME PROPERTIES OF MERCURY	25
	A. Physical Properties	25
	B. The Fermi Surface of Mercury -- Nearly Free Electron Approximation	25
	C. Possible Cyclotron Orbits in Mercury	31
	D. Results of Other Experiments on Mercury	31
CHAPTER IV	EXPERIMENTAL PROCEDURE AND APPARATUS	36
	A. Crystal Growth, Handling, and Storage	36
	B. X-Ray Orientation	39
	C. Cyclotron Resonance Spectrometers	41
	D. The Magnetoresistance Rig	43
	E. Magnet, Dewar, and Pumping System	46
CHAPTER V	EXPERIMENTAL RESULTS	48
	A. Cyclotron Resonance Results and Orbit Assignment	48
	B. Magnetoresistance Results	62
	C. Quantum Oscillations of the Microwave Surface Impedance	70
CHAPTER VI	DISCUSSION OF THE EXPERIMENTAL RESULTS	74
	A. An Ellipsoidal Fit to the Cyclotron Resonance Data	74
	B. A Cylindrical Fit to the Quantum Oscillation Data	76
	C. Comparison of the Data with the Nearly-Free-Electron Approximation	80
	1. Cyclotron Resonance Data	80
	2. Magnetoresistance Data	82
	3. Quantum Oscillation Data	83
	D. Comparison of the Data with the Relativistic-Augmented-Plane-Wave Approximation	84
	E. A Discussion of the Possible Effects of the Curved Sample Surface on the Cyclotron Resonance Signals	87
	F. Conclusions	88
BIBLIOGRAPHY		91

LIST OF TABLES

		PAGE
Table 1	Possible Cyclotron Orbits in Mercury	33
Table 2	Card Listing of the Ellipsoidal-Fit Computer Program	77

LIST OF FIGURES

FIGURE		PAGE
1	A Simple Extended Fermi Surface	12
2	Relationship Between $\vec{v}$ and $\vec{H}$ in Equation (II-10)	16
3	Calculated Absorption Curve for Infinite Relaxation Time	17
4	Relationship Between the Open-Orbit Direction and $\vec{J}$ in Equation (II-13)	22
5	The First Brillouin Zone of Mercury	26
6	The First-Zone Hole Surface of Mercury (Nearly-Free-Electron Approximation)	29
7	Possible Modifications of the Fermi Sphere Caused by the Lattice Potential	30
8	Model Showing Possible Closed Orbits (Top) and Open Orbits (Bottom) for Magnetic-Field Directions in the Trigonal Plane	32
9	Crystal-Growing Apparatus	37
10	X-Ray Apparatus	40
11	Block Diagram of the Cyclotron Resonance Spectrometer	42
12	8-mm. Cavity Showing Crystal-Growing Apparatus	44
13	Magnetoresistance Sample Holder	45
14	Cyclotron Resonance Subharmonics from One Azbel - Kaner Resonance	49
15	Cyclotron-Resonance Signals from Two Groups of Carriers	50
16	A Cyclotron Resonance Trace Using the Varian Spectrometer	51
17	Cyclotron Effective Mass Results for a Sample Surface Oriented Near the Trigonal Plane	54
18	Angular Range Over Which Orbits Remain Closed for Magnetic-Field Directions in the Trigonal Plane	56
19	Cyclotron Effective Mass Results at 69.6 Gc./sec.	58

FIGURE		PAGE
20	Cyclotron Effective Mass Results from Two Similarly-Oriented Samples	59
21	Cyclotron Effective Mass Results from a Sample Oriented as Shown in the Stereogram	61
22	Transverse Magnetoresistance Rotation Diagram	63
23	Magnetoresistance Rotation Diagrams for a Sample Tilted at Three Different Angles	65
24	Stereographic Projection Showing the Planes Corresponding to the Faces of the First Brillouin Zone	66
25	Magnetoresistance Results Projected on the Trigonal Plane	67
26	Dependence of the Magnetoresistance on Magnetic-Field Strength	69
27	Oscillations of the Microwave Surface Impedance	71
28	Surface Impedance Oscillation Frequencies Observed in the Sample Whose Orientation is Shown in Figure 17	73
29	Ellipsoidal Fits to Cyclotron Mass Data from the Electron Lenses	78
30	An Ellipsoidal Fit to the 4-mm. Cyclotron Mass Data	79
31	Cylindrical Fits to the Quantum Oscillation Data	81
32	Band Structure Results from Relativistic-Augmented-Plane-Wave Calculation	85
33	Intersection of the Fermi Surface with the Brillouin Zone Faces, RAPW Approximation	86

## CHAPTER I

INTRODUCTION

The first cyclotron resonance experiment in metals was performed by Fawcett (1956) in tin and copper. The most useful experimental geometry for a cyclotron resonance experiment in metals was proposed by Azbel' and Kaner (1956), who predicted that subharmonic resonances would exist because of the presence of a microwave skin depth. Subharmonic resonances were subsequently observed in tin by Kip, Langenberg, Rosenblum, and Wagoner (1957). The first cyclotron resonance experiment to report a detailed study of the anisotropy of the cyclotron effective mass, and to identify those masses with orbits on the Fermi surface, was an experiment on copper by Kip, Langenberg, and Moore (1961). Detailed cyclotron resonance results have since been reported in bismuth (Khaikin, Mina, and Edel'man, 1963), sodium and potassium (Grimes and Kip, 1963), copper (Koch, Stradling, and Kip, 1964), antimony (Datars and Vanderkooy, 1964), gold (Langenberg and Marcus, 1964), aluminum (Spong and Kip, 1965), cadmium (Galt, Merritt, and Klauder, 1965, and Shaw, Eck, and Zych, 1966), and zinc (Shaw, Sampath, and Eck, 1966).

In a metal with a multiply-connected Fermi surface, knowledge of the existence of open orbits, and of the range of magnetic-field directions for which they exist, can be extremely useful in ascertaining the connectivity of the surface and the size and orientation of connecting arms. This information can be obtained from magnetoresistance experiments using single-crystal samples. A review paper by Fawcett (1964) surveys

the experiments that have been done, and the results obtained.

When this experiment was started, no detailed information was available about the Fermi surface of mercury. Anomalous skin effect results had been reported by Pippard (1947), and de Haas - van Alphen effect measurements had been made on unoriented crystals by Verkin, Lazerev, and Rudenko (1951), and on crystals oriented using their magnetic anisotropy by Shoenberg (1952). Gustafson, Mackintosh, and Zaffarano (1963) had completed a positron-annihilation experiment on liquid and solid mercury. Mercury could be obtained commercially in a very pure form, which made it feasible to attempt a cyclotron resonance experiment. The results of this experiment, along with the knowledge obtained from a magnetoresistance experiment, were expected to yield detailed information about the Fermi surface of mercury. The appearance of oscillations in the microwave surface impedance, which have been identified as quantum oscillations, has permitted a further extension of the knowledge of the Fermi surface gained from these experiments.

## CHAPTER II

THEORYA. Motion of an Electron in Electric and Magnetic Fields

When an electron is acted upon by electric and magnetic fields, the force on the particle is given by the Lorentz equation,

$$\vec{F} = e(\vec{E} + \frac{1}{c} \vec{v} \times \vec{H}), \quad (\text{II-1})$$

where the first term shows the response to an electric field, and the second to a magnetic field. Using de Broglie's relation for the dependence of energy on wave number,

$$E = \frac{p^2}{2m} = \frac{\hbar^2 k^2}{2m},$$

$$\vec{F} = \frac{d\vec{p}}{dt} = \hbar \dot{\vec{k}} = e(\vec{E} + \frac{1}{c} \vec{v} \times \vec{H}). \quad (\text{II-2})$$

First consider the effect of a uniform electric field only. Here  $\hbar \dot{\vec{k}} = e \vec{E}$ , so that in the absence of collisions between electrons and defects in the crystal lattice, the momentum of the electrons increases linearly with time. This is equivalent to a motion of the whole Fermi sphere in  $\vec{k}$ -space. In the presence of lattice defects, an equilibrium current density is established, which can be described by a small shift of the Fermi surface in the direction of current flow.

In a constant magnetic field, the electron experiences a force normal to both the magnetic field direction and to its direction of motion. It then follows a helical orbit, spiralling about the magnetic

field direction. The representative point of the electron moves around the Fermi surface at the intersection of the Fermi surface with a plane normal to  $H$ . For a free electron, the representative point moves around the Fermi surface at the cyclotron frequency,

$$\omega_c = \frac{e H}{m c} .$$

For other than free electrons, we define the "cyclotron effective mass" using

$$\omega_c \equiv \frac{e H}{m_c^* c} . \quad (\text{II-3})$$

Note that this is not the same as the dynamical effective mass of the electron, given by

$$\frac{1}{m^*} = \frac{1}{\hbar^2} \frac{\partial^2 E}{\partial k^2} .$$

The cyclotron effective mass is a property of an orbit, while the dynamical effective mass is a property of a particular electronic state.

A useful geometrical representation of the cyclotron frequency is the following. If an electron is described as a wave with wave-number  $k$ , then the group velocity of that wave is given by

$$v_g = \frac{\partial \omega}{\partial k} = \frac{1}{\hbar} \frac{\partial E(k)}{\partial k} .$$

For an anisotropic medium, this can be written:

$$\vec{v}(k) = \frac{1}{\hbar} \vec{\nabla}_k E(\vec{k}) . \quad (\text{II-4})$$

The representative point of the electron, rotating around the Fermi surface at frequency  $\omega_c$  in a plane perpendicular to  $\vec{H}$ , makes one complete rotation in a time

$$T = \frac{2\pi}{\omega_c} = \frac{c\hbar}{eH} \oint \frac{dk}{v_{\perp}} . \quad (\text{II-5})$$

where  $v_{\perp}$  is the component of  $\vec{v}$  in the plane perpendicular to  $\vec{H}$  at the point  $\vec{k}$ . Here we have used equation (II-2) for an electron in a constant magnetic field. Equation (II-4) can be written:

$$v_{\perp} = \frac{1}{\hbar} \frac{\partial E}{\partial k_{\perp}} , \quad (\text{II-6})$$

where  $k_{\perp}$  is the component of  $\vec{k}$  in the plane of the orbit, and normal to the Fermi surface.

$$\begin{aligned} m_c^* &= \frac{eH}{\omega_c c} \\ \text{but } \frac{1}{\omega_c} &= \frac{c\hbar}{2\pi eH} \oint \frac{dk}{v_{\perp}} \text{ from (II-5),} \\ m_c^* &= \frac{eH}{c} \frac{c\hbar}{2\pi eH} \oint \frac{dk}{v_{\perp}} \\ &= \frac{\hbar^2}{2\pi} \oint \frac{dk_{\perp}}{dE} dk \text{ using (II-6),} \\ &= \frac{\hbar^2}{2\pi} \frac{\partial A}{\partial E} , \end{aligned} \quad (\text{II-7})$$

where  $A$  is the area of the orbit in  $\vec{k}$ -space in the plane normal to  $\vec{H}$ .

Equation (II-4) shows that the velocity of an electron in real space is perpendicular to a surface of constant energy, the Fermi surface. Under the action of the Lorentz force, in a constant magnetic field, the

value of  $k_H$ , the component of  $\vec{k}$  parallel to  $\vec{H}$ , is unchanged, and is a constant of the motion. In a plane perpendicular to  $\vec{H}$ ,  $\vec{k}$  changes along curves of constant energy, i.e., on the Fermi surface. Let  $\vec{k}_\perp$  be the two-dimensional wave vector in the plane normal to  $\vec{H}$ , and  $\vec{p}$  be the vector describing the orbit in real space in a plane normal to  $\vec{H}$ . Then we can write

$$\dot{\vec{k}}_\perp = \frac{e}{c} \dot{\vec{p}} \times \vec{H}.$$

Thus, as the representative point rotates around the Fermi surface in  $\vec{k}$ -space, the electron in real space describes an orbit which has the same shape, but is rotated by  $\pi/2$  about the magnetic field direction, and changed in size by a factor  $c/eH$ .

Since the electrons move in periodic orbits with frequency  $\omega_c$ , it might be expected that these orbits lead to a set of discrete energy levels, quantized in units of  $\hbar \omega_c$ . In the presence of a magnetic field, the classical Hamiltonian for a free electron takes the form

$$H = (\vec{p} - \frac{e}{c} \vec{A})^2 / 2m,$$

where  $\vec{A}$  is the vector potential. The electrons in the magnetic field must satisfy the Schrödinger equation,

$$\frac{1}{2m} \left( \frac{\hbar}{i} \vec{\nabla} - \frac{e}{c} \vec{A} \right)^2 \psi = E\psi.$$

If we take  $\vec{H}$  in the  $z$  direction and choose a gauge where

$$\vec{A} = (0, H_x, 0),$$

Schrödinger's equation becomes

$$-\frac{\hbar^2}{2m} \nabla^2 \psi + \frac{ie\hbar}{mc} H_x \frac{\partial \psi}{\partial y} + \frac{e^2}{2mc^2} H_x^2 x^2 \psi = E\psi \quad (\text{II-8})$$

Following Ziman (1964), equation (II-8) has the solution

$$\psi(x, y, z) = u(x)e^{i(\beta y + k_z z)}.$$

This leads to an equation for u:

$$\frac{\partial^2 u}{\partial x^2} + \left( \frac{2m}{\hbar^2} \left( E - \frac{\hbar^2}{2m} k_z^2 \right) - \left( \beta - \frac{eH}{\hbar c} x \right)^2 \right) u = 0$$

Letting  $E' = E - \frac{\hbar^2 k_z^2}{2m}$ , and rearranging,

$$-\frac{\hbar^2}{2m} \frac{\partial^2 u}{\partial x^2} + \left( \frac{eH}{mc} x - \frac{\hbar\beta}{m} \right)^2 u(x) = E' u(x),$$

which is the equation for a simple harmonic oscillator, of frequency  $\omega_c = \frac{eH}{mc}$ , centered on the point  $x = \hbar\beta/m\omega_c$ . The energy levels of the oscillator are given by:

$$E = \left( n + \frac{1}{2} \right) \hbar\omega_c + \frac{\hbar^2}{2m} k_z^2.$$

The electron orbits are quantized in the plane perpendicular to the magnetic field direction, but motion along the magnetic field direction is unchanged. In a magnetic field, the electrons condense on a discrete set

of energy levels in  $\vec{k}$ -space, in such a way that the average density of states is unchanged. Since the energy levels depend on  $\vec{H}$  (through  $\omega_c$ ), the distance between levels increases as the magnetic field increases, and the number of levels inside the Fermi surface decreases.

## B. Cyclotron Resonance

### 1. Physical Picture

Since electrons spiral about the direction of a constant magnetic field with a frequency equal to the cyclotron frequency, it is possible to cause resonance with a microwave field of suitable frequency. In metals, the carrier density is so high (approximately  $10^{22}$  /cm.<sup>3</sup>) that the microwave field only penetrates to a depth of the order of the classical skin depth  $\delta$ , given by

$$\delta = \left( \frac{mc^2}{2\pi ne} \right)^{1/2}.$$

For a microwave frequency  $f \approx 10^{10}$  sec.<sup>-1</sup>, and in a magnetic field of 10 kG, the skin depth is of the order of  $10^{-5}$  cm., while the orbiting carriers have an orbit radius of the order of  $10^{-3}$  cm. The proper experimental geometry was first suggested by Azbel' and Kaner (1956). If the sample is mounted so that it forms one wall of a microwave cavity, and a constant magnetic field is parallel to the sample surface, the carriers spiralling in and out of the skin depth resonate with the microwave electric field if they return to the skin depth at the same point in an r.f. period during each cycle of their rotation. Consequently, resonance will occur whenever  $\omega_c = \omega/n$ , where  $\omega$  is the applied r.f. frequency, and  $n$  is an integer.

This region, in which the radius of the carrier orbit is much greater than the skin depth, is called the anomalous skin effect region. If the microwave frequency is constant, and the magnetic field is slowly changed, cyclotron resonance signals will occur for  $H_c = m_c^* c\omega/e$ , and for  $H = H_c/n$ . The signals at  $H_c/n$  are called subharmonic resonances because there the cyclotron frequency is a subharmonic of the microwave frequency. In order for the resonance to occur, the electron should rotate through at least one orbit before it is scattered, i.e., the condition  $\omega_c \tau > 1$  must hold, where  $\tau$  is the relaxation time of the electrons. Experiments are performed at liquid helium temperatures, and on single crystals with few impurities in order to assure that  $\tau$  is large. This experiment should not be confused with cyclotron resonance in semiconductors (see, e.g., Dresselhaus, Kip, and Kittel, 1955, and Dexter, Zeiger, and Lax, 1956), where carrier densities are low. In semiconductors, resonance between the carriers and the r.f. field takes place when the cyclotron frequency of the orbiting carriers is equal to the microwave frequency, and subharmonic resonances only occur because of a non-spherical Fermi surface. In metals, subharmonics occur because of the existence of the skin depth, and for any shape Fermi surface. The presence of the skin depth also accounts for another difference in the two types of cyclotron resonance -- at resonance the power absorbed is a maximum in semiconductors, but a minimum in metals. In both cases the conductivity is a maximum at resonance, but in metals the skin depth is an inverse function of the conductivity, so that the net effect is an absorption minimum.

The origin of the resonance effect has been described by Pippard (1962). The electric current at the point  $\vec{r}$  at time  $t$ , which is caused by an electron moving with velocity  $\vec{v}$ , depends on the past history of that electron. If it was given an impulse by the microwave field at regular intervals in the past, its motion at time  $t$  will be a function of these impulses, and of a relaxation time that governs the remaining effect of past impulses. This decay will be exponential, with time constant  $\tau$ , and will be represented by a term of the form  $\exp. (-2\pi/\omega_c \tau)$ . During each revolution, the electron also gains or loses in phase with the oscillating field, by an amount  $(2\pi\omega/\omega_c)$ . The conductivity will then contain a term of the type

$$F = \sum_{n=0}^{\infty} \exp. \left\{ -\frac{2\pi n}{\omega_c \tau} + i \frac{2\pi \omega n}{\omega_c} \right\}$$

$$= \left\{ 1 - \exp. \left[ -\frac{2\pi}{\omega_c \tau} - i \frac{2\pi \omega}{\omega_c} \right] \right\}^{-1}.$$

It is the oscillations of the function  $F$  that cause the resonance effect. Pippard (1962) has also shown that in the extreme anomalous limit ( $\ell \gg \delta$ , where  $\ell$  is the carrier's mean free path), the surface impedance varies as  $\sigma^{-1/3}$  and is given by

$$Z_{\infty}(H) = \alpha Z_{\infty}^0(o) F^{-1/3}$$

where  $Z_{\infty}^0(o)$  is the surface impedance in the extreme anomalous limit at zero magnetic field, and  $\alpha$  is a constant factor, of order 1.

For an ellipsoidal or spherical energy surface, the cyclotron

frequency is the same for all electrons on the surface, and thus the cyclotron mass is the same for all orbits. An expression for the cyclotron mass was formulated by Shockley (1953). For an ellipsoidal energy surface,

$$E = \frac{p_x^2}{2m_x} + \frac{p_y^2}{2m_y} + \frac{p_z^2}{2m_z}.$$

In a magnetic field with direction cosines  $\alpha$ ,  $\beta$ ,  $\gamma$ ,

$$m^* = \left\{ \frac{m_x m_y m_z}{(m_x \alpha^2 + m_y \beta^2 + m_z \gamma^2)} \right\}^{1/2}, \quad (\text{II-9})$$

and measurement of the effective mass in a few directions allows the energy surface to be completely determined. Our results will show that the second zone electron lenses in mercury can be approximated (rather poorly) by an ellipsoid of revolution. For a Fermi surface of arbitrary shape, the cyclotron mass is a function of  $k_H$ , and resonance signals result from extremal orbits on the Fermi surface, where there are a large number of carriers with approximately the same cyclotron mass. Figure 1 shows an extended Fermi surface, containing two extremal sections. For the two orbits shown,  $\partial A / \partial k_H = 0$ , and these are called stationary orbits because the electron has zero velocity along the magnetic field direction, returning to the skin depth at the same point in real space as it goes around its orbit again and again.

If the r.f. electric field is polarized along the direction of the constant magnetic field, another extremal section contributes to resonance. Here the r.f. currents flow in the same direction as the constant magnetic field, and perpendicular to the direction of motion of

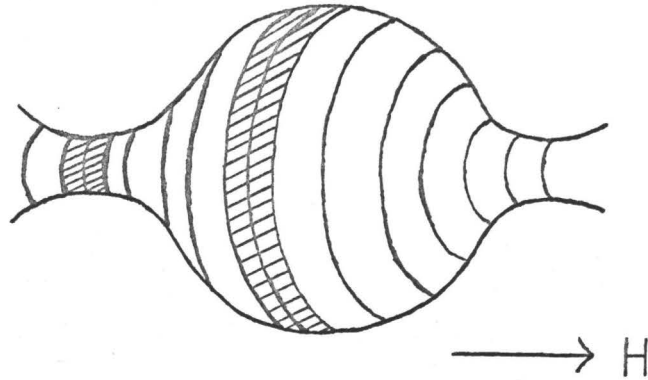


FIGURE 1

## A Simple Extended Fermi Surface

the electrons in the stationary orbits described. These electrons will not be very effective in carrying current along the magnetic field direction. A resonance effect will come from carriers near elliptic limiting points on the Fermi surface, which are moving along the magnetic field direction with a velocity  $v \lesssim v_F$ , where  $v_F$  is the Fermi velocity. Because of their large velocity along the magnetic field direction, limiting point resonances require flat, smooth sample surfaces, and a magnetic field that is accurately aligned parallel to the sample surface.

When the magnetic field direction is not parallel to the sample surface, stationary orbits are still effective in producing resonances, although the number of carriers contributing to the resonance will be reduced, since the electrons on the edge of the effective zone, which have small velocities along the magnetic field direction, will be less effective in producing resonance. This reduces the mass spread of the effective electrons, however, which may tend to sharpen the resonance. Since the microwave field changes in phase as well as in amplitude as the electron goes deeper into the metal, this change of phase may broaden the resonance line, or cause it to split (since the Fermi surface is centrally symmetric, there will be the same number of electrons spiralling up into the skin depth as are spiralling down out of it). The effects of field tipping are discussed in several papers (see, for example, Koch, Stradling, and Kip, 1964, Langenberg and Marcus, 1964, and Spong and Kip, 1965) and several theories have been advanced to explain the observed effects. In this experiment the sample surface is not perfectly flat, since we are using the central portion of the free crystal surface, and no tilting effects have been observed. The effect of a rough crystal surface is simply a lowering of the effective mean free path of the electrons, an effect that will be much more pronounced for limiting point resonances than for stationary orbits.

## 2. Azbel' - Kaner Theory

Azbel' and Kaner (1956) first proposed cyclotron resonance experiments in metals with the magnetic field parallel to the sample surface,

and their theoretical calculation (Azbel' and Kaner, 1958) has become the standard reference. Theoretical calculations were also done by Heine (1957), and by Mattis and Dresselhaus (1958). Heine formulated the problem using Pippard's "ineffectiveness concept" (only those carriers whose direction of motion is within an angle  $\beta \delta/\ell$  with the surface are effective in transport of current, where  $\beta$  is of order unity), which results in an answer very similar to that obtained by Azbel' and Kaner. Mattis and Dresselhaus solved the Boltzmann transport equation, with the boundary condition of specular reflection at the sample surface. Specular reflection is a rather artificial boundary condition, since the reflection is almost surely diffuse, but since the electrons actually participating in resonance are not reflected at all, the final result is changed only slightly from the result using diffuse reflection. They have also attempted a quantum mechanical formulation of the problem which gives similar results at low magnetic fields, but at higher fields predicts that the dominant behaviour will be a de Haas - van Alphen type of variation of the surface impedance.

Azbel' and Kaner (1958) determined the surface impedance tensor  $Z_{\mu\nu}$  under anomalous skin effect conditions, and with a magnetic field applied parallel to the sample surface. The surface impedance tensor  $Z_{\mu\nu}$  was defined by

$$E_{\mu}(0) = \sum_{\nu=1}^2 Z_{\mu\nu} J_{\nu},$$

where  $Z_{\mu\nu} = R_{\mu\nu} + i X_{\mu\nu}$

and  $\mu, \nu = x, y$ .

$E_\mu(0)$  is the electric field in the absence of a magnetic field. They solved for  $E_\mu(H)$ , using Maxwell's equation, and the Boltzmann transport equation for the relationship of a perturbation  $f_1$  to the equilibrium Fermi distribution  $f_0$ :

$$\vec{j} = -\frac{2e}{h} \int \vec{v} f_1 dp_x dp_y dp_z$$

$$f_0 = \frac{1}{1 + \exp. (\epsilon - \epsilon_f)/kT}$$

$$i\omega f_1 + v_z \frac{\partial f_1}{\partial z} - \frac{e}{c} (\vec{v} \times \vec{H}) \cdot \frac{\vec{\partial} f_1}{\partial p} + \left( \frac{\partial f_1}{\partial t} \right)_{\text{coll.}} = e \vec{E} \cdot \vec{v} \frac{\partial f_0}{\partial \epsilon}$$

where  $f_1(z=0, v_z > 0) = 0$  is the condition for diffuse reflection of electrons at the surface of the metal. A relaxation time was introduced:

$$\left( \frac{\partial f_1}{\partial t} \right)_{\text{coll.}} = \frac{f_1}{\tau}.$$

In the resonance region, the surface impedance of the metal was found to depend on terms like:

$$A_{\mu\nu} = \frac{8e^2}{3h^3} \int_0^{2\pi} \frac{n_\mu n_\nu}{K} \frac{d\phi}{1 - \exp. (-2\pi i \omega / \Omega - 2\pi / \Omega \tau)} \quad (\text{II-10})$$

where  $\Omega = \omega_c$  in our notation,

$K$  = the Gaussian curvature of the Fermi surface,

and the relationship between the velocity of the electrons on the Fermi surface and the angle  $\phi$  is shown in Figure 2.

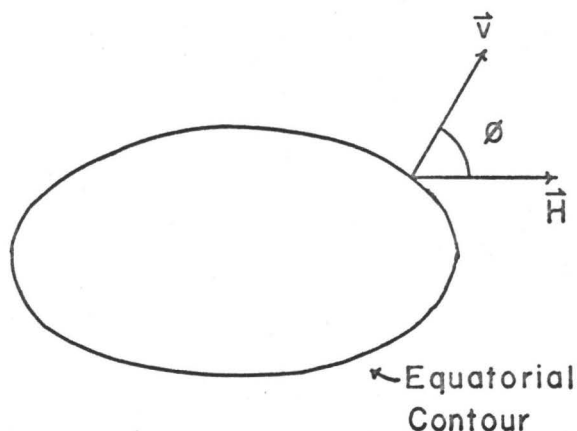


FIGURE 2

Relationship Between  $\vec{v}$  and  $\vec{H}$  in Equation (II-10)

$$\begin{aligned}\vec{v} &= v_x \vec{i} + v_y \vec{j} \\ &= v \cos \phi \vec{i} + v \sin \phi \vec{j} \\ &= n_x v \vec{i} + n_y v \vec{j}\end{aligned}$$

Integration is around the equatorial contour on the Fermi surface, since these are the electrons whose velocity is parallel to the sample surface. Note that if the Fermi surface is open in all planes perpendicular to  $\vec{H}$ , then  $\omega_c = 0$  and the resonance vanishes. The dependence on  $K$  can be seen using Pippard's "ineffectiveness concept". If  $K$  is small, then there are a large number of electrons whose direction of motion lies within an angle  $\beta \delta/l$  of the sample surface, resulting in a large resonance effect. Chambers (1956) has pointed out that a second term should be added to Equation (II-10) to take into account the contribution of internal, non-resonant electrons on the equatorial contour of the Fermi surface. If the

Fermi surface is not a simple closed, convex surface, there may be several points on the equatorial contour with a common value of  $\phi$ . These points can be divided into bounding points, points where the electron is either farthest from or nearest to the surface, and internal points, where the orbit has an intermediate extremal value. An internal point cannot contribute to resonance, because if this point were inside the skin depth, the electron would be reflected from the surface. Internal points do, however, contribute a non-resonant term to the surface impedance.

Using Azbel' and Kaner's result, Kip, Langenberg, and Moore (1961) calculated the absorption curve shown in Figure 3, for an infinite relaxation time.

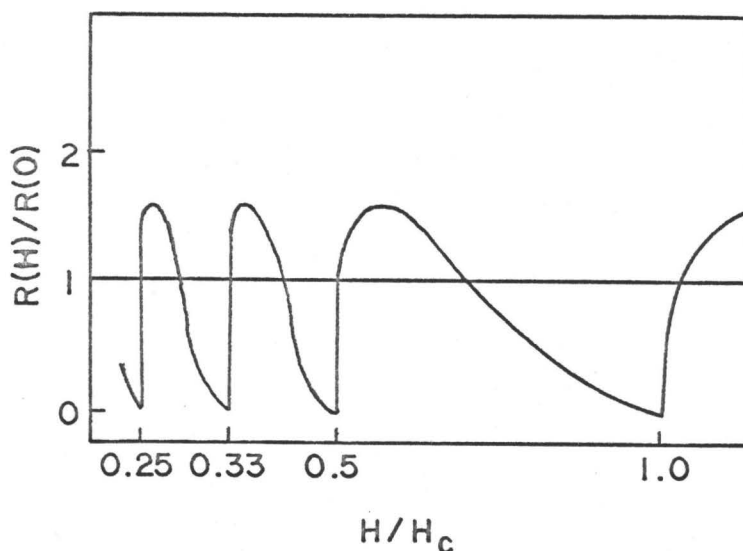


FIGURE 3

Calculated Absorption Curve for Infinite Relaxation Time

Note the sharp minima of the resonance signals. For a non-infinite relaxation time, the size of the resonance signals increases from zero to a maximum at the fundamental resonance, and the sharp corner is rounded off. The usual experimental arrangement is to measure  $dR/dH$ , not  $R(H)$ , and the derivative maxima are used to compute the cyclotron mass instead of the cross-over point, because of the shape of the resonance signals. Because the derivative enhances higher frequencies, the fundamental is no longer the largest resonance, and the signals grow from zero to a maximum, then decrease towards the fundamental, as shown in Figure 16. This effect has been used to estimate  $\omega\tau$  (Kip, Langenberg, and Moore, 1961).

### C. Transverse Magnetoresistance

A closed Fermi surface can support only closed electron or hole orbits. An electron orbit surrounds a region of filled states, and its representative point moves in a clockwise direction about the magnetic field direction, while a hole orbit surrounds a region of empty states, and its representative point moves in a counterclockwise direction (the definitions are reversed if the surface is a hole surface). If, however, a Fermi surface is open (is connected to the Fermi surface in adjacent zones in the extended zone scheme), it may support open and extended orbits as well. In order for these orbits to have any effect on the galvanomagnetic properties, the electron must be able to travel several times around a closed orbit, or traverse a reasonable distance along an open orbit before it is scattered. In order to make sure that this is the case, experiments are performed in the high field region, i.e., where  $\omega_c\tau \gg 1$ .

The representative point of an electron moves along the open orbit in  $\vec{k}$ -space from zone to zone, and since its real space velocity is perpendicular to the Fermi surface, its average velocity in real space will be perpendicular to the open orbit direction in  $\vec{k}$ -space. Thus, an open orbit in the x direction corresponds to electrons moving in the y-z plane. Because of the magnetic field, the representative point in  $\vec{k}$ -space is confined to a plane perpendicular to the magnetic field direction, and it is also constrained to move on the Fermi surface, so that an open orbit will not exist, even though the surface is connected to adjacent surfaces in  $\vec{k}$ -space, unless both conditions are fulfilled simultaneously. An open surface that supports no open orbits for any direction of  $\vec{H}$  is shown by Fawcett (1964).

Periodic open orbits are further classified as primary, secondary, tertiary, etc., depending on whether the orbit uses repeatedly one, two, or three basic arms of the Fermi surface. An example of a primary open orbit is the (100) orbit in mercury, which uses the same arm repeatedly.

Two-dimensional aperiodic open orbits are sometimes generated for a range of angles of magnetic field direction centered on a symmetry axis. They are called aperiodic because there is no regularly repeated set of arms making up the orbit, and two-dimensional because they are represented by an area on a stereogram.

Since mercury is divalent, with one atom per unit cell, the Fermi surface contains as many electrons as there are states in the first Brillouin zone, and so mercury must be a compensated metal. In other words, the number

of filled electron states in the second zone must equal the number of empty states, or holes, in the first zone.

The conductivity tensor  $\sigma_{ij}$  is defined by:

$$J_i = \sigma_{ij} E_j,$$

where  $\sigma_{ij}$  can be expressed as a series expansion of the dimensionless parameter  $\gamma$  (see Lifshitz, Azbel', and Kaganov, 1957):

$$\gamma = \frac{1}{\omega_0 \bar{\tau}} = \frac{m_0 c}{e \bar{\tau}} \frac{1}{H}$$

where  $\omega_0$  is the free electron cyclotron frequency and  $\bar{\tau}$  is an average relaxation time around the cyclotron orbit.

Then the expansion is given by:

$$\sigma_{ij} = a_{ij}^0 + a_{ij}^1 \gamma + a_{ij}^2 \gamma^2 + \dots$$

For a compensated metal, and in the absence of open orbits, the resistivity tensor has been calculated by Fawcett (1964), and is given by:

$$\begin{aligned} \text{Lt. } \rho_{ij} &= \begin{vmatrix} \sim \gamma^{-2} & \sim \gamma^{-2} & \sim \gamma^{-1} \\ \sim \gamma^{-2} & \sim \gamma^{-2} & \sim \gamma^{-1} \\ \sim \gamma^{-1} & \sim \gamma^{-1} & \sim \gamma^0 \end{vmatrix} \\ \gamma \rightarrow 0 & \\ H \rightarrow \infty & \\ &= \begin{vmatrix} \sim H^2 & \sim H^2 & \sim H \\ \sim H^2 & \sim H^2 & \sim H \\ \sim H & \sim H & \sim H^0 \end{vmatrix} \end{aligned} \quad (\text{II-11})$$

where  $\sim H^2$  means that the highest order term in the expansion of  $\rho_{xx}$  in terms of  $H$  is a term in  $H^2$ .

The magnetoresistance is given by:

$$\frac{\nabla\rho(H)}{\rho(0)} = \frac{\rho_{ii}(H) - \rho_{ii}(0)}{\rho_{ii}(0)} . \quad (\text{II-12})$$

Thus the transverse magnetoresistance,  $\nabla\rho_{xx}/\rho_0$  or  $\nabla\rho_{yy}/\rho_0$ , is quadratic in H in the high field limit, while the longitudinal magnetoresistance,  $\nabla\rho_{zz}/\rho_0$ , saturates.

The resistivity tensor with the magnetic field along the z direction and an open orbit along the x direction is:

$$\begin{aligned} \text{Lt. } \rho_{ij} &= \begin{vmatrix} \sim\gamma^{-2} & \sim\gamma^{-1} & \sim\gamma^{-1} \\ \sim\gamma^{-1} & \sim\gamma^0 & \sim\gamma^0 \\ \sim\gamma^{-1} & \sim\gamma^0 & \sim\gamma^0 \end{vmatrix} \\ \gamma \rightarrow 0 & \\ H \rightarrow \infty & \\ &= \begin{vmatrix} \sim H^2 & \sim H & \sim H \\ \sim H & \sim H^0 & \sim H^0 \\ \sim H & \sim H^0 & \sim H^0 \end{vmatrix} . \end{aligned} \quad (\text{II-13})$$

Here  $\rho_{xx}$  is quadratic in H, while  $\rho_{yy}$  and  $\rho_{zz}$  saturate.

Suppose a current is set up in a sample, and a large constant magnetic field is set, point-wise, at different orientations around the current axis. The interpretation of such a rotation diagram follows from Equations (II-11) and (II-13). The resistivity will have a large value ( $\propto H^2$ ) except where the magnetic field direction is perpendicular to an open orbit direction, when the resistivity drops to a sharp minimum ( $\propto H^0$ ). An example of this type of data is shown in Figure 22. Since an open orbit conducts

only in the plane perpendicular to the orbit direction, it will have most effect when  $\vec{J}$  is perpendicular to the open orbit. If  $\vec{J}$  is in the x-y plane, with an open orbit along the x axis and H along the z axis (see the diagram below), then the magnetoresistance is given by:

$$\rho_{\alpha\alpha} = (C_{xx}^0 + C_{xx}^2 H^2) \cos^2 \alpha + C_{yy}^0 \sin^2 \alpha . \quad (\text{II-14})$$

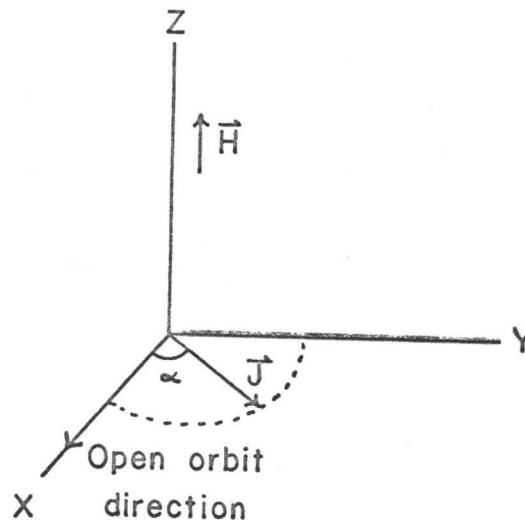


FIGURE 4

Relationship Between The Open Orbit Direction and  $\vec{J}$  In Equation (II-14)

Thus open orbits that cause the largest dip on a rotation diagram are those in which the current direction is perpendicular to the open orbit direction, and saturation only occurs for  $\alpha = \pi/2$ .

#### D. Quantum Oscillations of the Microwave Surface Impedance

Quantum oscillations of the microwave surface impedance with a large constant magnetic field parallel to the sample surface have been predicted theoretically by Mattis and Dresselhaus (1958) and by Azbel' (1958). The origin of such oscillations is the same as the de Haas - van Alphen oscillations of the magnetic susceptibility and the de Hass - Shubnikov oscillations of the D.C. impedance. It was pointed out in part A that a constant magnetic field causes quantization of the electrons into energy levels in a plane perpendicular to the magnetic field direction. As the magnetic field is increased, these levels pass through the Fermi surface, and the electrons on the levels go to levels inside the Fermi surface, causing a periodic change in the density of states at the Fermi level. It is this periodic change in the density of states that causes an oscillation of the microwave surface impedance. The energy levels were found to occur at energies

$$E = (n + \frac{1}{2}) \hbar \omega_c,$$

and orbits differing by  $\hbar \omega_c$  in energy will be separated by  $\frac{dA}{dE} \hbar \omega_c$  in area. Using equation (II-7), we can write:

$$\frac{\partial A}{\partial E} = \frac{2\pi m^* c}{\hbar} = \frac{2\pi eH}{\hbar \omega_c c},$$

so the orbits are separated by  $\frac{2\pi eH}{\hbar c}$  in area, and are given by:

$$A = (n + \frac{1}{2}) \frac{2\pi eH}{\hbar c}.$$

Then the periodicity of the surface impedance oscillations is related to the cross-sectional area of the Fermi surface,

$$\Delta \left( \frac{1}{H} \right) = \frac{2\pi e}{\hbar c A}, \quad (\text{II-15})$$

where  $A$  is the cross-sectional area of extremal sections of the Fermi surface.

If the magnetic field direction is tilted with respect to the sample surface, electrons which have  $\bar{v}_H \neq 0$  will spiral quickly out of the skin depth, and do not contribute effectively to the conductivity. In this case, only stationary orbits ( $\bar{v}_H = 0$ ) will contribute to the oscillations.

## CHAPTER III

SOME PROPERTIES OF MERCURYA. Physical Properties

Mercury is a heavy, shiny, silver metal, which is liquid at room temperature. It has a specific gravity of 13.546, and a melting point of  $-38.87^{\circ}\text{C}$ . Its atomic weight is 200.61, and its atomic number is 80. It can be readily purified by distillation, and high purity mercury (99.99999% pure) is commercially available. Mercury oxidizes very slowly in air, and forms amalgams with many other metals. The single crystals look much like molten mercury, and have a smooth, shiny surface. The solid is very soft, even at liquid nitrogen temperatures, and requires great care in handling so as not to damage the surface. Mercury is a good conductor of heat and electricity.

B. The Fermi Surface of Mercury -- Nearly Free Electron Approximation

Mercury is a divalent atom, which crystallizes in a trigonal lattice, with one atom per unit cell. Thus the first Brillouin zone, which can hold a maximum of two electrons, has the same volume as the free electron Fermi sphere. At  $5^{\circ}\text{K}$ , the lattice constant of mercury has been measured to be  $2.9963\text{\AA}$ , with a rhombohedral angle of  $70^{\circ} 44.6'$  (Barrett, 1957). An angle of  $60^{\circ}$  corresponds to a face-centered cubic lattice. The Brillouin zone was constructed following Jones (1960), and is shown in Figure 5, with the free electron Fermi sphere intersecting the L-faces.

Because mercury is a non-cubic crystal, care must be taken in converting directions in real space to directions in reciprocal space.

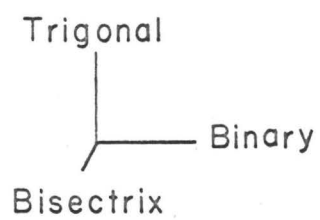
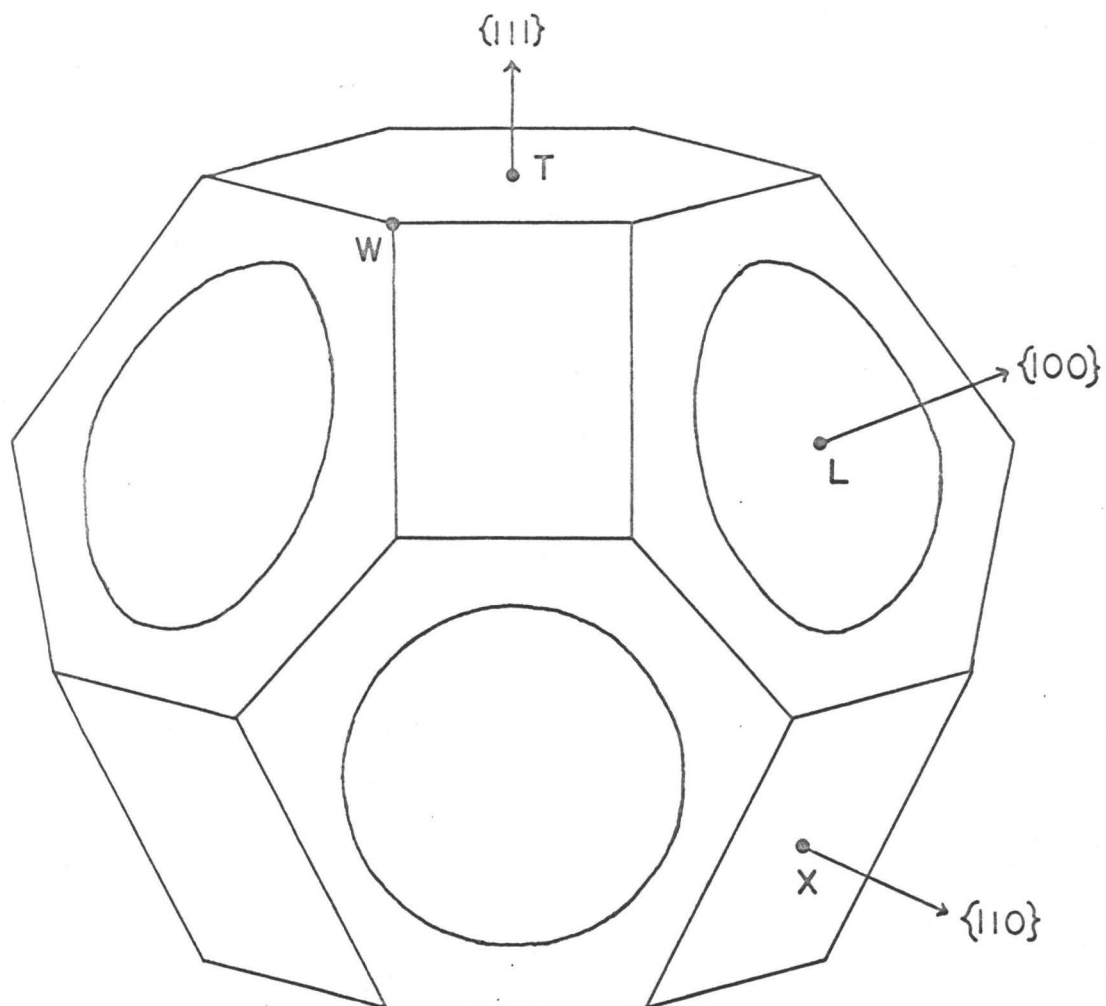


FIGURE 5

THE FIRST BRILLOUIN ZONE OF MERCURY

The following convention will be used. A direction in the crystal lattice is specified by  $[l, m, n]$ . A reciprocal lattice point is designated  $(l, m, n)$ , and is perpendicular to the set of planes  $(l, m, n)$  in the direct lattice. The orientation of a direction in real space with respect to the Brillouin zone is determined by finding the normal to the plane in reciprocal space containing all the reciprocal lattice vectors whose dot product with  $[l, m, n]$  vanishes. The three orthogonal directions, trigonal, binary, and bisectrix, are specified by  $[111]$ ,  $[1\bar{1}0]$ , and  $[11\bar{2}]$  in real space, and by the same indices,  $(111)$ ,  $(1\bar{1}0)$ , and  $(11\bar{2})$  in reciprocal space. A set of equivalent directions in real space will be designated  $\langle l, m, n \rangle$ , and  $\{l, m, n\}$  represents a set of equivalent planes in real space, or a set of equivalent reciprocal lattice vectors.

A model of the Fermi surface has been constructed, using the nearly free electron or single-orthogonalized-plane-wave approximation, and following the construction described by Harrison (1960). This approximation is the same as the free electron approximation except that there are connectivity modifications at the zone faces. The edges are not rounded off to cut the zone boundaries at right angles, as required by Bragg reflection. The cyclotron effective mass of an orbit in this approximation is simply the total angle through which the orbit moves divided by  $360^\circ$ , the angle through which an electron travelling in a circular orbit would move, since the effective mass of an electron going around a sphere without reflections is unity.

The free electron Fermi sphere cuts through the six L-faces of the Brillouin zone, but does not quite touch the T- or X-faces (single-OPW approximation). This results in electron lenses in the second zone, and a first-zone hole surface composed of multiply connected tubes that will support open orbits in both the  $\{100\}$  and binary directions. A model of the first-zone hole surface is shown in Figure 6. The model is shown in the same orientation as the Brillouin zone in Figure 5. Black areas on the model are areas where the surface is joined to other parts of the extended-zone surface. The model was built on a framework the size of the first Brillouin zone, and fills a volume of reciprocal space approximately twice that of one Brillouin zone. The single-OPW Fermi surface supports only three closed orbits -- around the second-zone electron lenses, a bow-tie shaped hole orbit across the narrow dimension of the X-faces, and a hole orbit across the T-faces starting at W and going across to the opposite corner.

The model is extremely thin at the center of the T- and X-faces, as shown in Figure 7. The T-face is just slightly farther from the center of the zone than is the X-face. The dotted lines show a possible Fermi surface after the lattice potential is taken into account. Note that it predicts that the Fermi surface will touch both the T- and X-faces.

A band-structure calculation for mercury has been done by Keeton and Loucks (1966), using a Relativistic Augmented Plane Wave method (Loucks, 1965). This calculation predicts that the Fermi surface touches the zone boundary at the center of both the T- and X-faces (see Figure 33).

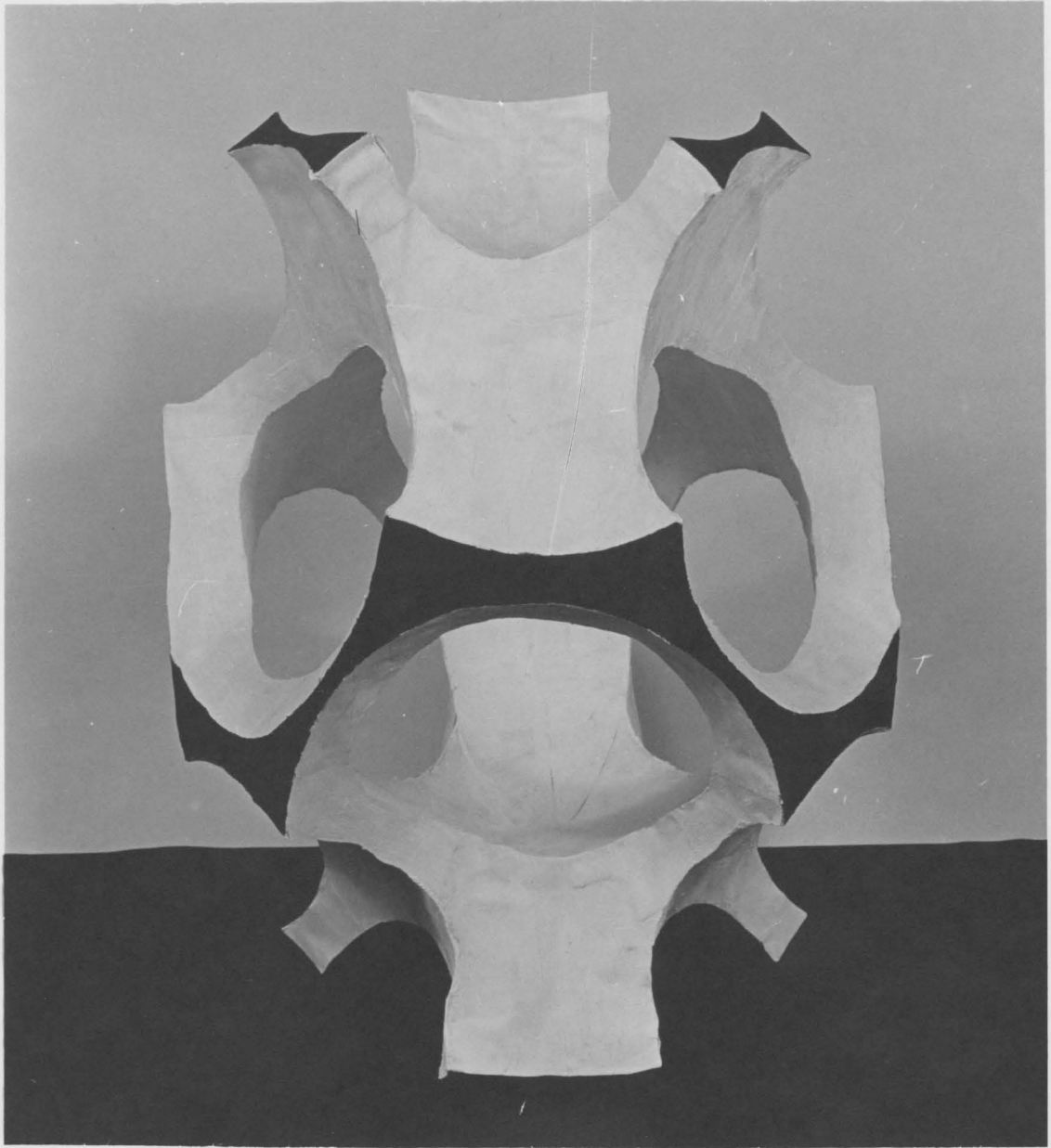


FIGURE 6

THE FIRST-ZONE HOLE SURFACE OF MERCURY  
(NEARLY-FREE-ELECTRON APPROXIMATION)

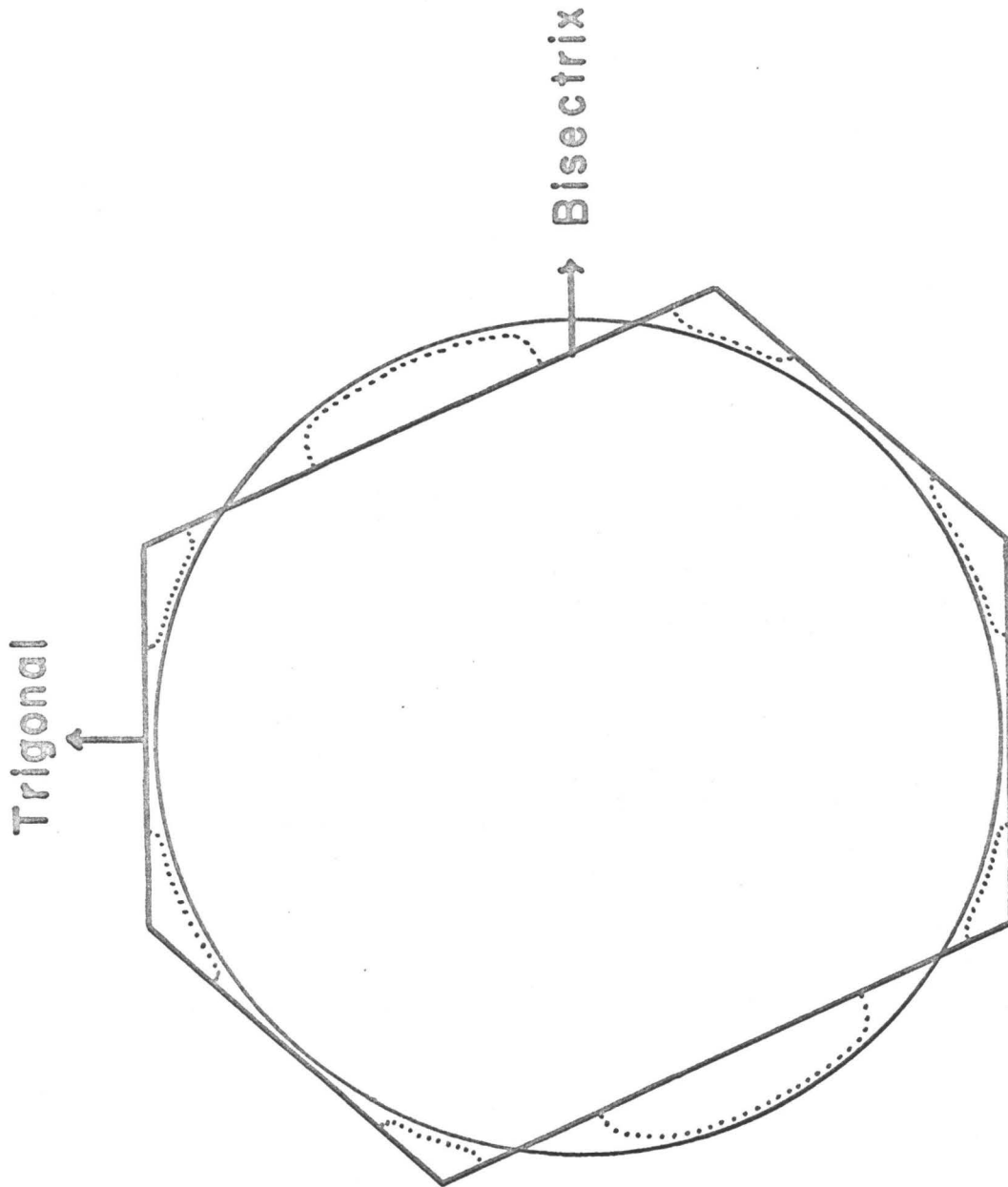


FIGURE 7  
POSSIBLE MODIFICATIONS OF THE FERMI SPHERE  
CAUSED BY THE LATTICE POTENTIAL

### C. Possible Cyclotron Orbits in Mercury

If we assume a Fermi surface that touches both the T- and X-faces, as predicted by Keeton and Loucks (1966), then several closed orbits are possible. Some of these orbits are shown in Figure 8, where the areas of contact with the zone boundary are shown as a small circle on the T-face, and as rounded rectangles on the X-faces (Keeton and Loucks predict that the rectangles will have the width shown, but will be nearly square). Note that the actual orbits will be considerably more rounded at the intersection of adjacent Fermi spheres than is shown on this model. A description of the possible cyclotron orbits in mercury is given in Table 1. The orbits are named to correspond with the convention used by Brandt and Rayne (1966) and by Keeton and Loucks (1966).

### D. Results of Other Experiments on Mercury

Until recently, very little was known about the Fermi surface of mercury. Pippard (1947) reported anomalous skin effect results. De Haas - van Alphen effect measurements were made by Verkin, Lazerev, and Rudenko (1951) on unoriented crystals, and by Shoenberg (1952) on crystals oriented using their magnetic anisotropy. Oscillations, of minimum frequency  $f\left(\frac{1}{H}\right) = 7.2 \times 10^5$  gauss, showed that mercury had a small, anisotropic section on its Fermi surface. From a study of the resistivity of mercury, Ziman (1960) concluded that the area of the Fermi surface of mercury was a little less than half the area of the free-electron Fermi sphere. Gustafson, Mackintosh, and Zaffarano (1963), in a positron annihilation experiment, compared the angular distribution of photon coincidences from

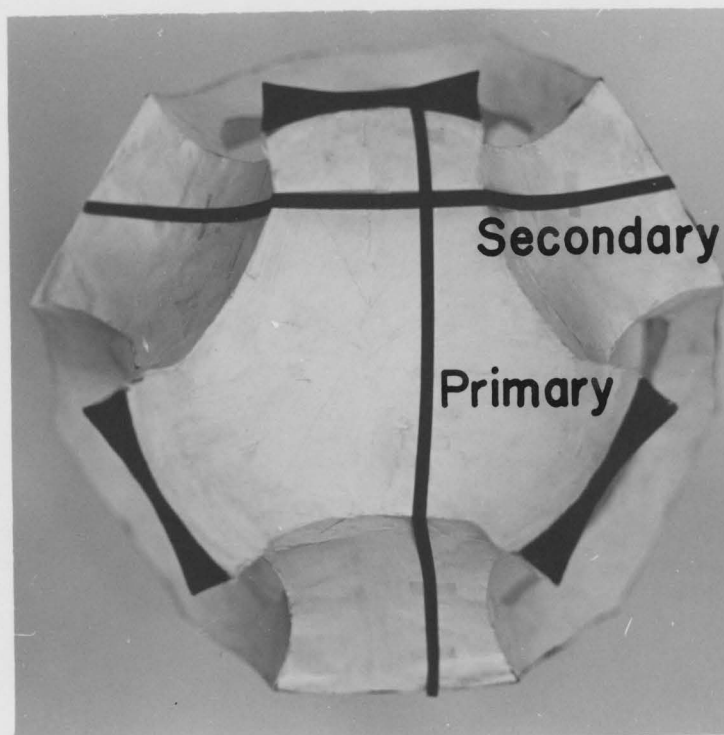
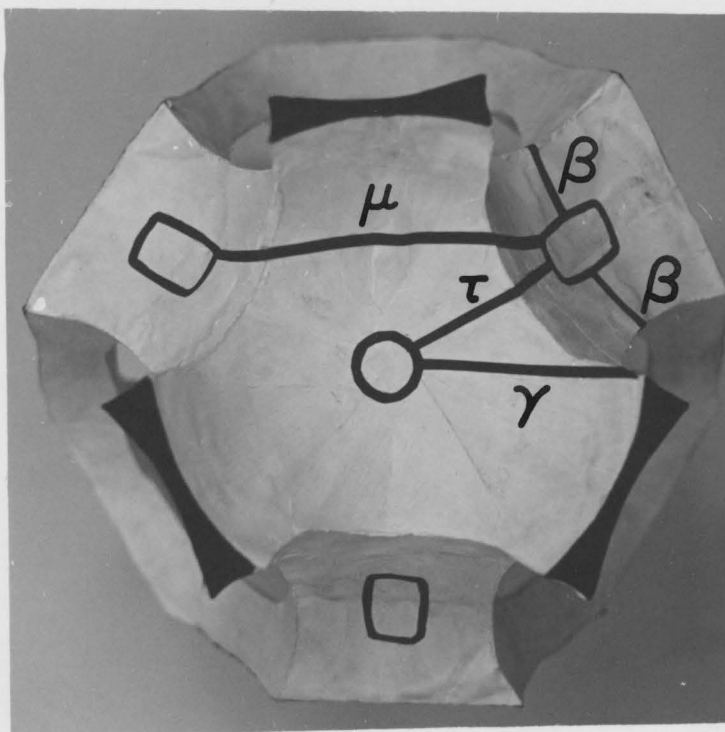


FIGURE 8  
MODEL SHOWING POSSIBLE CLOSED ORBITS (TOP) AND OPEN ORBITS (BOTTOM)  
FOR MAGNETIC-FIELD DIRECTIONS IN THE TRIGONAL PLANE

Table 1  
Possible Cyclotron Orbits in Mercury

Orbit Designation	Description
$\alpha$	Electron orbit, around the second-zone lenses. It should be possible to see this orbit for any orientation.
T-face neck	Electron orbit, around the neck where the F. S. touches the T-faces. Should be seen when the magnetic field is along the trigonal direction; orientation is probably very critical.
X-face neck	Electron orbit, around the neck where the F. S. touches the X-faces. Should be seen when the magnetic field is along a {110} direction; orientation is probably very critical.
$\beta$	Hole orbit, around the cylinders that lie along the long sides of the X-faces. These cylinders should give closed orbits even at a fairly large angle from the cylindrical axis.
$\tau$	Hole orbit, coming out through a T-face neck, and down (or up) and in through an X-face neck. The minimum area of this orbit corresponds to a magnetic field in the binary direction and the orbit is closed for a small angular range about this direction.
$\gamma$	Hole orbit, half of the orbit across the T-face in the nearly-free-electron approximation. The minimum area corresponds to a magnetic field along the bisectrix direction (for a magnetic field rotating in the binary-bisectrix plane) and the orbit remains closed for a small angular range about this direction.

Table 1 (continued)

Orbit Designation	Description
$\mu$	Hole orbit, stretching from one X-face neck, across the T-face, to another X-face neck. The orbit is closed when the magnetic field is along the bisectrix direction and for a small angular range about this direction. When the magnetic field is rotated in the binary-bisectrix plane, the orbit has a minimum area at the bisectrix direction, and remains closed for a small angular range about this direction, the angular range depending on the size of the X-face necks.

liquid and solid mercury. The plot for the solid could be fitted very well by a parabola corresponding to two free electrons per atom, indicating that the Fermi surface in extended k-space did not depart significantly from a sphere. Brandt and Rayne (1965), using a de Haas - van Alphen effect torque magnetometer, measured the cross-sectional area of the  $\beta$  orbit, and found it to have a minimum area of  $0.0070 \text{ \AA}^{-2}$ , at a frequency corresponding closely to the frequency measured earlier by Shoenberg (1952). Their crystals were oriented using back-reflection Laué techniques. More recently, Brandt and Rayne (1966) have discovered two other sets of oscillations, corresponding to the electron lenses (the  $\alpha$  orbits), and to the  $\tau$  orbits. Measurements were made from 10 to 60 kilogauss, using both a torque magnetometer and an RF technique. Transverse magnetoresistance measurements in mercury have been reported by Dishman and Rayne (1966) and by Dixon and Datars (1965), and Datars and Dixon (1966). Results have shown open orbits along {100} directions and along the binary directions. The measurements have confirmed that mercury is a compensated metal.

## CHAPTER IV

EXPERIMENTAL PROCEDURE AND APPARATUSA. Crystal Growth, Handling, and Storage

Mercury crystals were grown from 99.99999% pure mercury supplied by the United Mineral and Chemical Corp. of New York. The growing rig is shown in Figure 9 (see also Figure 12). The sample holder was machined from Kel-F, and care was taken to make the window at the bottom of the narrow starter tube as thin as possible, usually about as thick as a piece of paper (Kel-F was chosen instead of teflon because its thermal expansion coefficient was closer to that of mercury). The sample holder sat on a copper cooling fin that was attached at the top to the cold side of a thermoelectric device (Frigistor model 1FB.08.15.E1). The hot side of the device was attached via a short copper sheet to the microwave cavity sitting above the pool of mercury in the holder. Silicone oil was smeared on each of the joints to improve thermal contact. The temperature was monitored during crystal growth with two thermocouples, one attached to the copper cooling fin just under the sample holder, and one attached to the copper sheet at the hottest point in the circuit. This last thermocouple gave warning when the hot junction of the Frigistor approached 100°C., its maximum operating temperature. Power for the Frigistor was supplied by a car battery with a large rheostat in series.

The sample holder was cleaned by soaking in nitric acid for several days, and washing with methyl hydrate. Mercury was transferred to the sample holder inside a dry box that had been filled with helium gas,

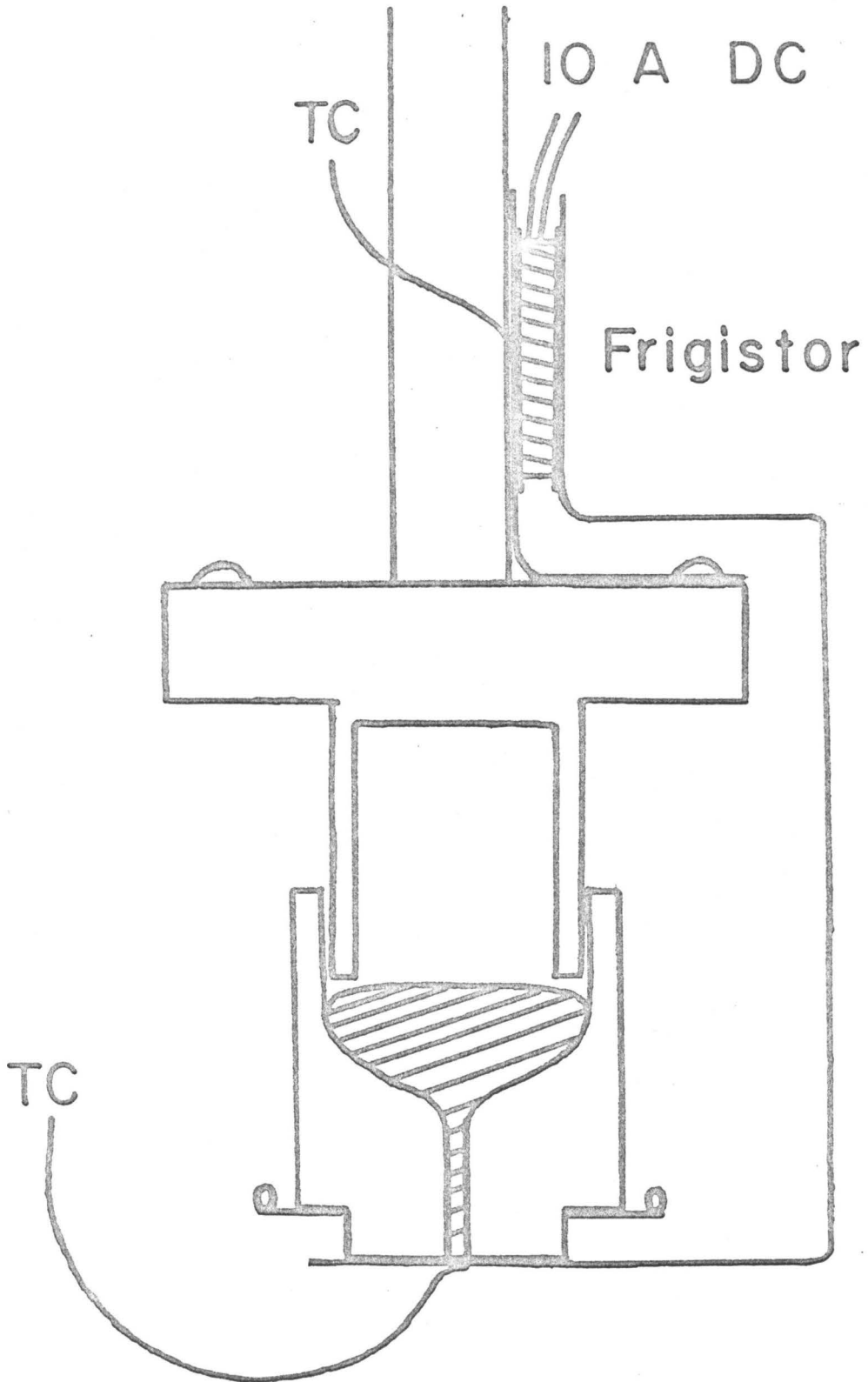


FIGURE 9

CRYSTAL-GROWING APPARATUS

and the sample holder was then mounted below the cavity, sitting on the copper cooling fin. A drop of silicone oil provided good thermal contact between the sample holder and the cooling fin. The rig was transferred from the dry box to the inner dewar of a double dewar system, and the air was quickly pumped out. During this pumping, any air bubbles in the starter tube were removed. The inner dewar was filled with helium gas at atmospheric pressure, the outer dewar was filled with liquid nitrogen, and the vacuum in the dewar's vacuum jacket was softened to about 0.1 mm. of Hg. by admitting air. The sample then started to cool down, and the Frigistor was switched on at about 5 amperes. Initially, the hot junction of the Frigistor was kept just below room temperature by varying the current. At about 8 amperes of current through the Frigistor (more for short sample holders, less for long ones), the whole rig was allowed to cool slowly through the freezing point of mercury ( $-38^{\circ}\text{C}.$ ). The rate of cooling was adjusted by changing the Frigistor current slightly until both the hot and cold thermocouples were cooling at about  $1^{\circ}\text{C}.$  per minute. There was a temperature difference between the two thermocouples of between 20 and 30 Centigrade degrees during the time of crystal growth. The Frigistor was switched off and the sample was allowed to cool to liquid nitrogen temperature as soon as the hot thermocouple reached the freezing temperature of mercury. During crystal growth great care was taken to minimize vibrations in the room. The dewar was wedged against one pole face of the magnet, and the crystals were grown at night after everyone had left the building.

The samples were stored between experiments in test tubes inside a storage dewar containing liquid nitrogen. They were not removed from the Kel-F sample holders. The shiny surface did not deteriorate noticeably when the crystals were stored with that surface toward the bottom of the test tube. Some samples were kept for more than a year. Whenever the crystals were removed from the dewar, care was taken to keep the shiny surface covered with liquid nitrogen, because out in the air the samples quickly became covered with frost.

#### B. X-Ray Orientation

The crystals were oriented using back reflection Laué techniques. The crystals were mounted on a goniometer using a barrel holder, as shown in Figure 10. A small orientation pin inside the barrel slid into a slot in the side of the sample holder, and a set-screw then held the sample holder firmly in the barrel. The goniometer was mounted inside a polystyrene ice bucket, which was in turn mounted on a platform that slid on the track of the x-ray machine. Long nylon screws held the goniometer mount, ice bucket, and platform firmly together. The bucket was filled with liquid nitrogen, and the liquid level was kept above the sample at all times. A plug of polystyrene (shown cross-hatched in the diagram) was carefully cut to fill the space between the mercury surface and the side of the ice bucket, so that the x-ray beam would not have to pass through the liquid nitrogen. Exposure time for the pictures was about three hours, and during this time a blower was kept on the outside of the bucket towards the film to keep a layer of frost from forming in that area. A dehumidifier

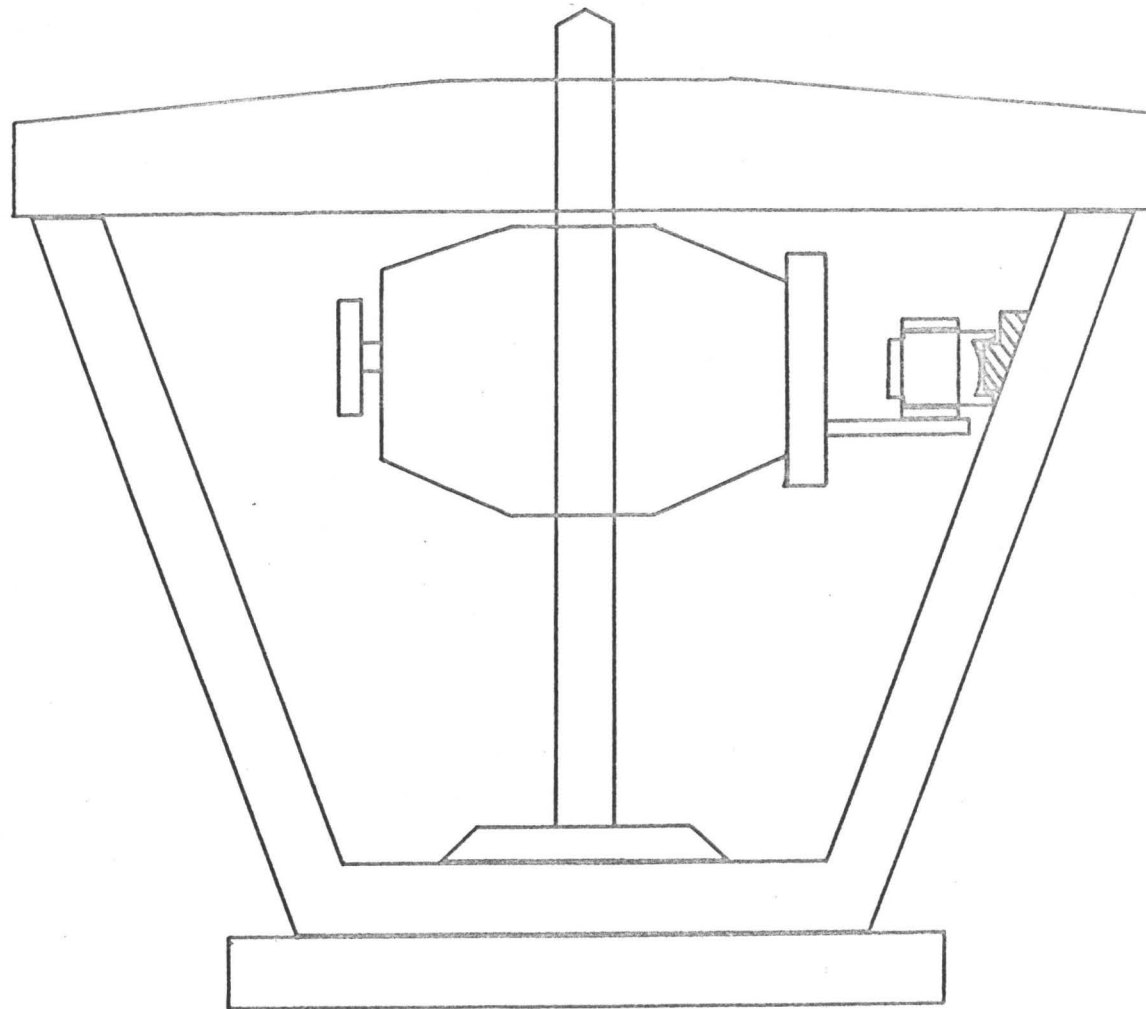


FIGURE 10

X-RAY APPARATUS

in the x-ray room was used to reduce humidity and frost.

### C. Cyclotron Resonance Spectrometers

The 4 mm. data and the early 8 mm. data were taken using the spectrometer shown in Figure 11. The microwave power generated by the klystron was propagated through 4 mm. or 8 mm. waveguide, through an isolator, an attenuator, and a frequency meter to a Magic Tee, where the power split, half going toward the sample cavity and half to a slide-screw tuner and matched load. The power reflected back from the cavity also split at the Magic Tee, half going toward the klystron, where it was lost in the isolator, and the other half going to the crystal detector. Similarly, half the power reflected back from the slide-screw tuner was lost in the isolator, and half went to the crystal detector. The bias of the detector crystal was set by adjusting the amplitude and phase of the signal reflected from the slide-screw tuner. The derivative of the resonance signal was detected by modulating the magnetic field with modulation coils on the pole faces of the magnet, and detecting the modulated absorption signal. The detection equipment consisted of a narrow-band amplifier and phase-sensitive detector. A D.C. output signal was recorded by a chart recorder. The klystron frequency was locked to the resonant frequency of the sample cavity by modulating the reflector voltage of the klystron at 10 Kc./sec. and detecting the 10 Kc./sec. signal reflected back to the crystal detector from the sample cavity. This was amplified and compared with the original 10 Kc./sec. signal in a phase-sensitive detector, which added a D.C. error signal to the reflector

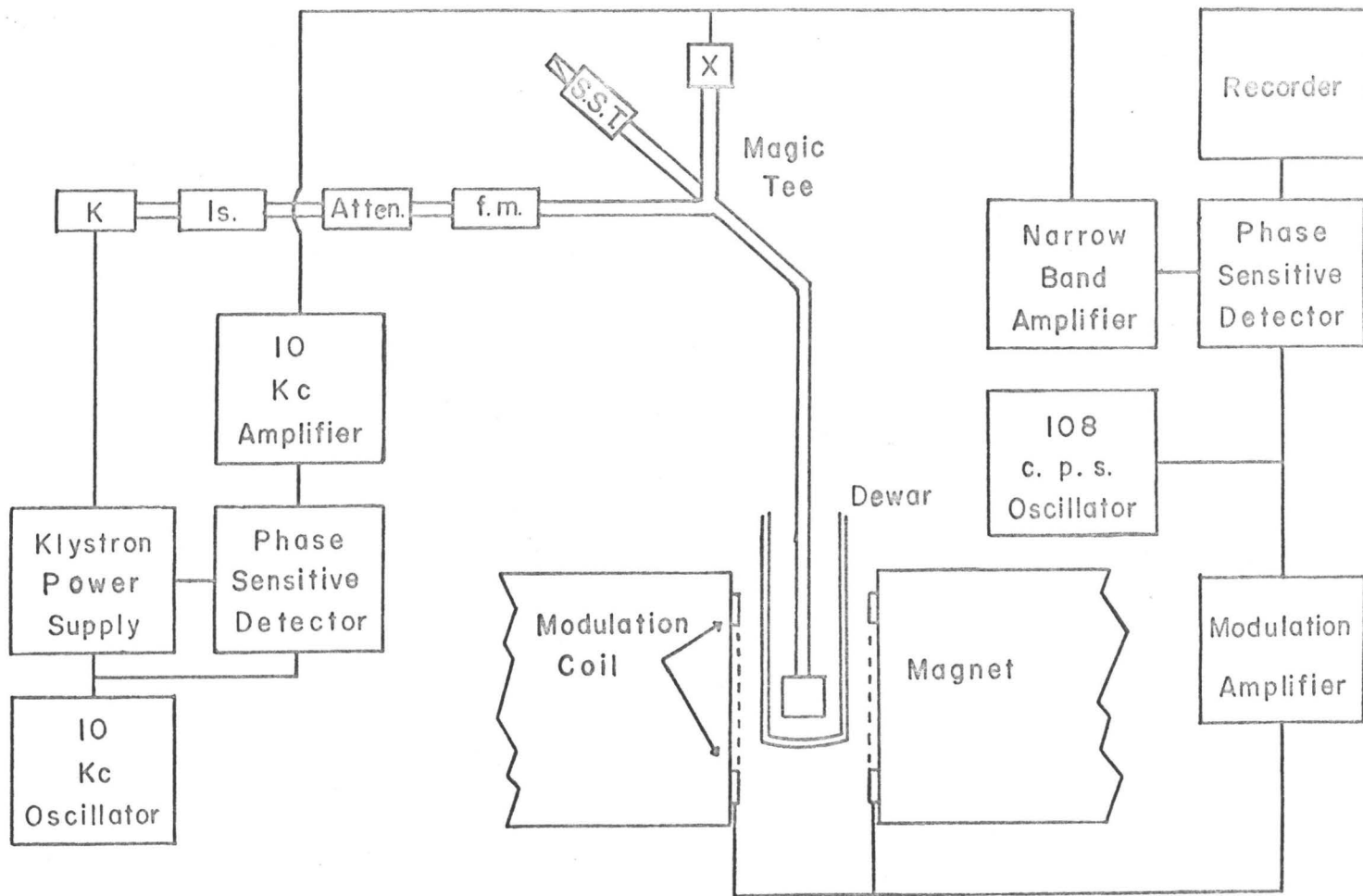


FIGURE 11

BLOCK DIAGRAM OF THE CYCLOTRON RESONANCE SPECTROMETER

voltage of the klystron to lock the klystron to the cavity frequency. The 4 mm. klystron was a Varian model VA-250, with an average power output of 35 mW. at 70 Gc./sec., and the 8 mm. klystron was an E.M.I. model R5146, with an average power output of 75 mW.

The data for samples number 21 and 22 were taken with a Varian model V-4503 E.P.R. Spectrometer, using the same sample cavities as before. This unit used a VA284B klystron oscillating at 35 Gc./sec. The typical power output from this klystron was 200 mW.

The 4 mm. microwave cavity was a cylindrical cavity that oscillated in the  $TE_{111}$  mode, and used a mode-splitting pin to separate the two  $TE_{111}$  modes. The 8 mm. cavity also oscillated in the  $TE_{111}$  mode. It was split into two parts halfway down the cylindrical wall, so that the bottom half could be rotated, using a small set of gears in such a way that the microwave electric field and the D.C. magnetic field remained at right angles to each other and in the sample plane. This cavity is shown in Figure 12. The thermoelectric device is visible above the cavity. The pin on the right of the cavity was used to align the sample holders with respect to the cavity. The sample formed the bottom wall of the cavity, and was held in place by a ring around the base of the sample holder, which was connected with nylon thread to a moveable rod at the top of the dewar.

#### D. The Magnetoresistance Rig

The magnetoresistance sample holder is shown in Figure 13. The sample was grown in a Kel-F holder, which was the long starter-tube section of a cyclotron resonance sample holder. The starter-tube section

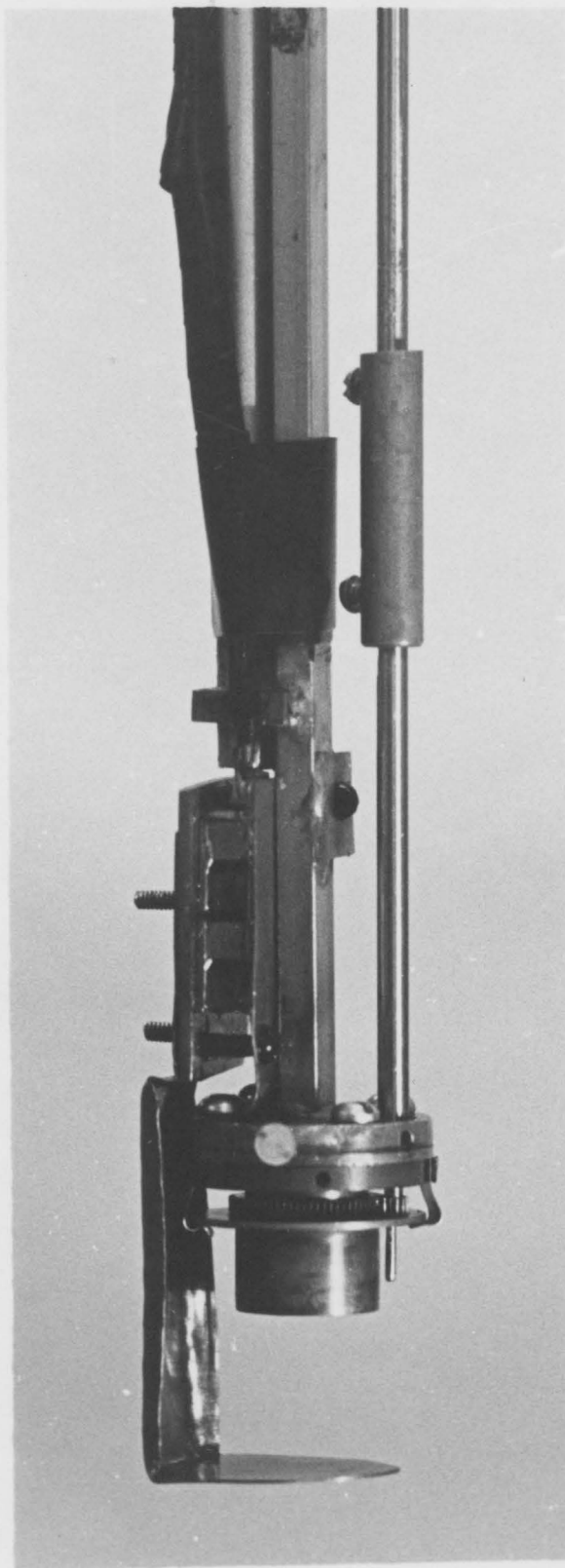
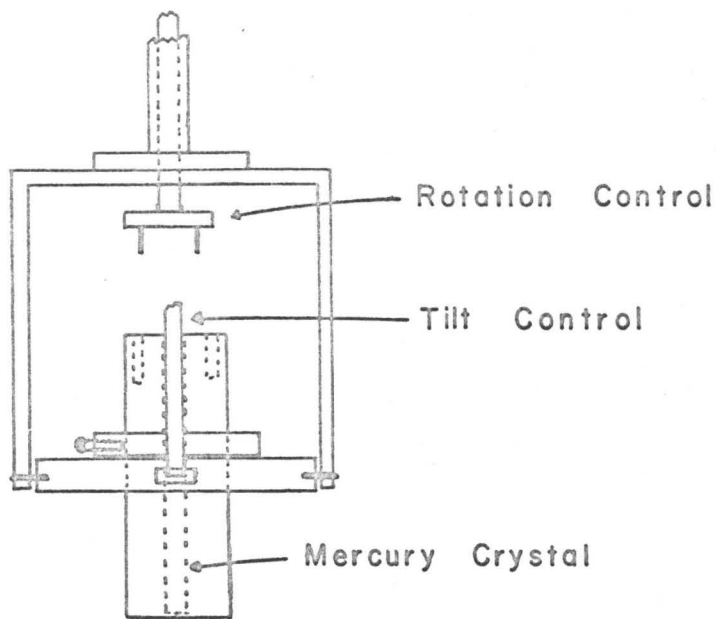
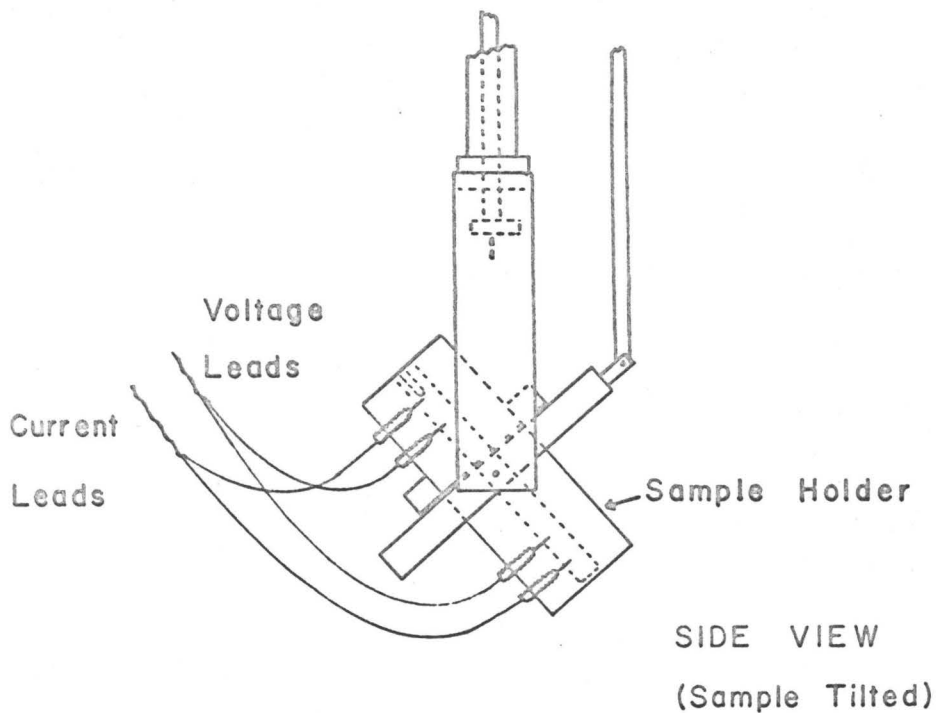


FIGURE 12

8-mm. CAVITY SHOWING CRYSTAL-GROWING APPARATUS



FRONT VIEW



SIDE VIEW  
(Sample Tilted)

FIGURE 13

MAGNETORESISTANCE SAMPLE HOLDER

was cut from the cyclotron resonance sample using a jeweller's saw. The sample holder shown in the diagram was 1 1/8 inches long and 35/64 inches in diameter. Electrical contact was made with the sample by drilling the final hole necessary for sharp contact probes after the crystal was grown, and then the probes were screwed into the previously threaded holes in the Kel-F holder. The contact probes were machined from small brass screws. The ring that holds the sample holder in place was made of Kel-F, and a nylon set-screw held the sample tight enough so that the spring in the leads would not cause motion during the experiment. The sample was rotated by moving it to a vertical position, lowering the rotation control into two holes drilled in the top of the Kel-F holder, and turning a calibrated dial at the top of the rig. Tilting was done accurately by pushing the tilt control rod downwards with a micrometer drive. D.C. current was supplied with a Harrison Lab Model 6248A power supply, and the voltage was measured with a Keithley Model 149 Milli-Microvoltmeter.

#### E. Magnet, Dewar, and Pumping System

The magnet was a twelve inch Pacific Electric Motor Electromagnet, with a 20 kilowatt power supply having a constant field-sweep control. The magnet produced a magnetic field of 20 kilogauss using 12" tips and a 2" gap, and 23 kilogauss with tapered tips and a 2" gap. The magnetic field was measured with a Rawson rotating-coil gaussmeter (Series 820, 1/10% accuracy) calibrated with a proton resonance probe. A marker was automatically put on the graph every thousand gauss.

The dewar was a stainless steel double dewar system, in which the tail section was not surrounded by liquid nitrogen. It was made by Hoffman Laboratories Inc., Newark, New Jersey.

A Balzers Duo 25 vacuum pump was connected to the inner dewar with a two-inch pumping line, with a short section of one-inch line at the top of each rig. In order to reach lower temperatures, a Speedivac model 1SC450B was put in parallel with the Balzers pump. This gave a temperature of about 1.22°K.

## CHAPTER V

EXPERIMENTAL RESULTSA. Cyclotron Resonance Results and Orbit Assignment

Cyclotron resonance signals with as many as twenty subharmonics have been observed. Examples of these signals are shown in Figures 14, 15, and 16. Figure 14 shows one Azbel' - Kaner resonance. The fundamental resonance, at 8.4 kG., is not shown; the subharmonic resonances are indicated with arrows. Figure 15 shows two resonances, with the different subharmonic sets indicated by two rows of arrows. Figure 16 shows an experimental trace taken with the Varian spectrometer, where the signal-to-noise ratio was greatly improved over earlier measurements, and small oscillations of the surface impedance are evident at high fields. These oscillations will be discussed in the last section of this chapter. Three Azbel - Kaner resonances are shown in Figure 16; their subharmonic sets are indicated by three rows of arrows. The large peak at 300 gauss was caused by the superconducting transition of the mercury sample, which resulted in a signal that saturated the spectrometer. Some of the subharmonics showed subsidiary maxima on the low-field side of the peaks, which are attributed to a slightly curved sample surface. The small peaks at 3950 gauss and 2610 gauss are examples of these subsidiary maxima, which are also evident in Figure 14. If these peaks are plotted on a graph of  $1/H$  versus the subharmonic number,  $n$ , they yield a straight line which crosses the  $n$ -axis at about  $n = -0.5$ , whereas a plot of the large peaks yields a straight line that crosses the  $n$ -axis between

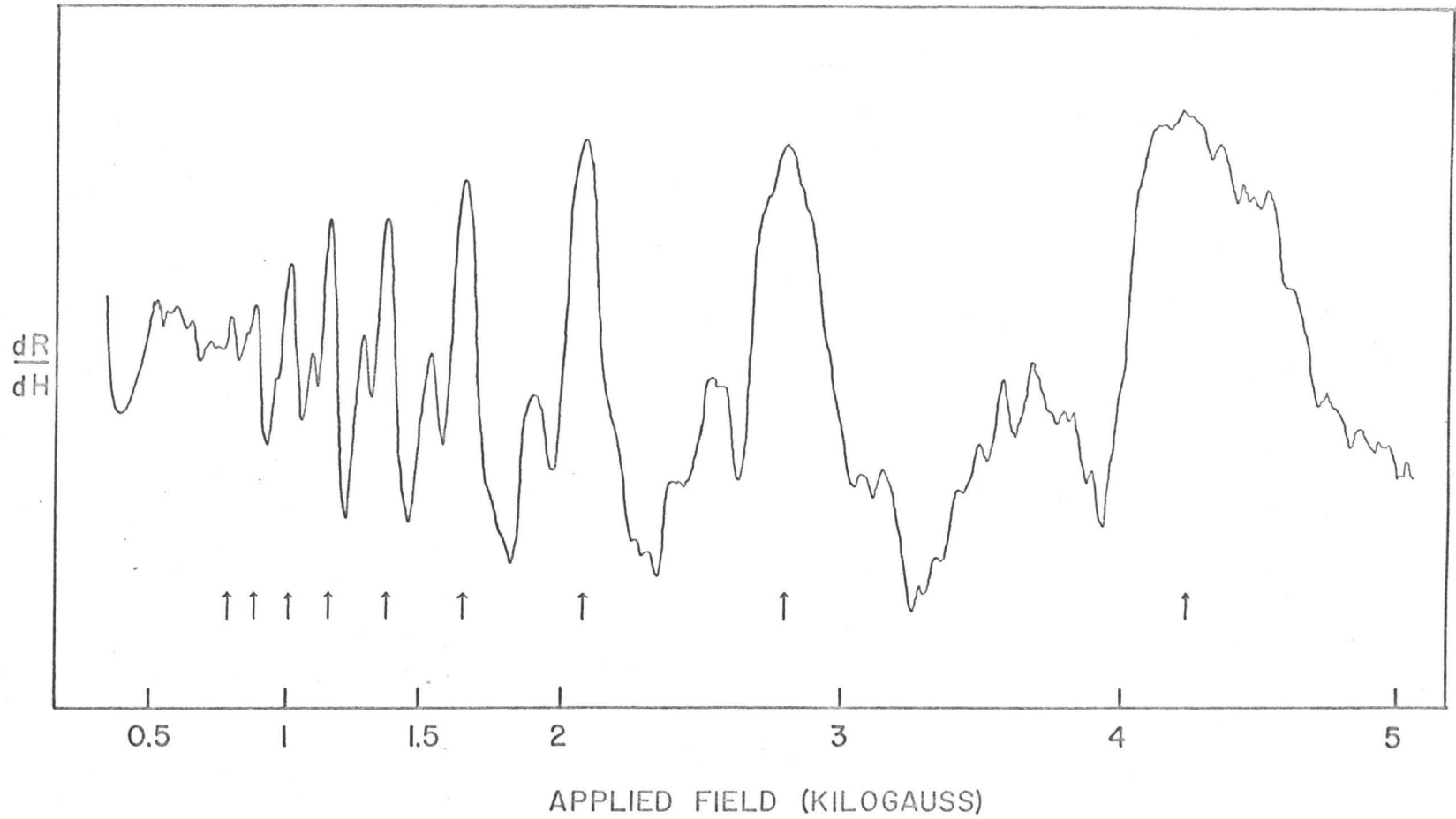


FIGURE 14

CYCLOTRON RESONANCE SUBHARMONICS FROM ONE AZBEL' - KANER RESONANCE

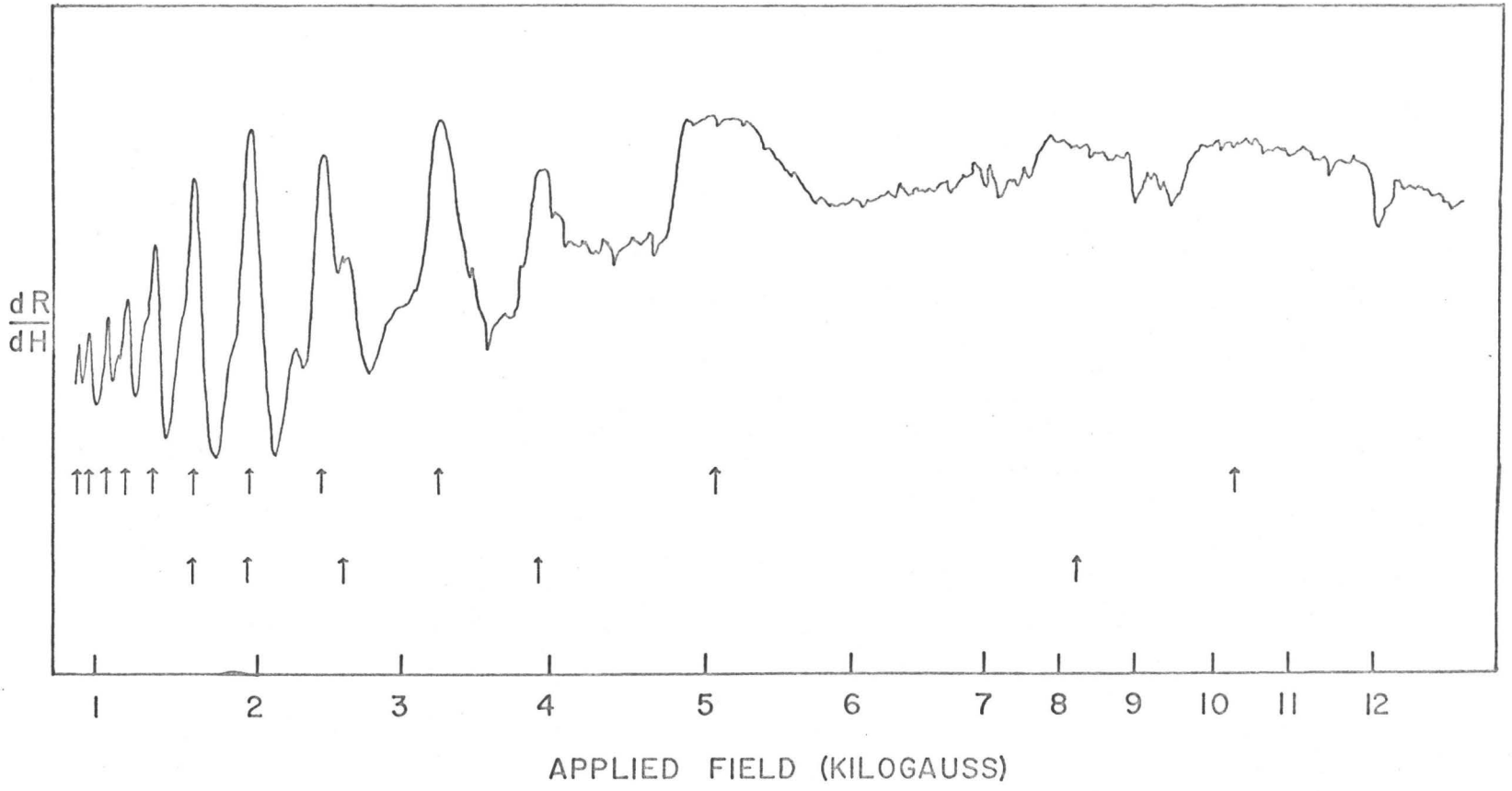


FIGURE 15

CYCLOTRON-RESONANCE SIGNALS FROM TWO GROUPS OF CARRIERS

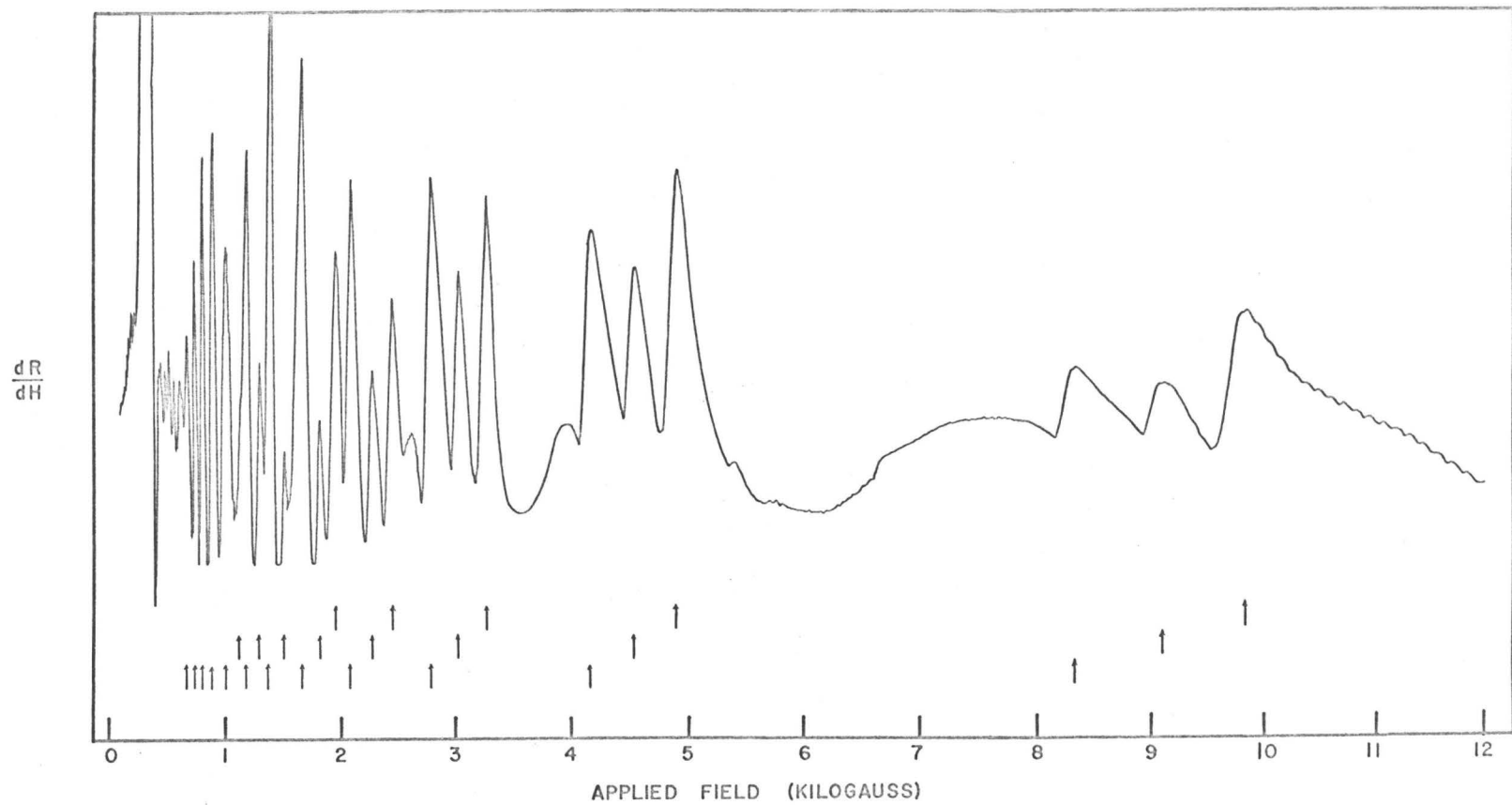


FIGURE 16

A CYCLOTRON RESONANCE TRACE USING THE VARIAN SPECTROMETER

$n = -0.05$  and  $n = +0.05$  for most of the resonances observed. This value at the intercept is called the phase shift of the resonance. The small peak at 5390 gauss was observed in many traces, falling between 4500 gauss and 6000 gauss depending on the direction of the magnetic field. Its origin cannot be explained at this time. The small increase in  $\frac{dR}{dH}$  at 6600 gauss was caused by changing the time constant of the spectrometer from 1/10 second to 1 second. This trace corresponds to the effective masses shown at  $32 \frac{1}{2}^\circ$  in Figure 17.

Since the mercury crystals were grown in situ, and the top surface of the crystal was then used to form the bottom wall of the microwave cavity, the sample surface was slightly curved. It was also extremely smooth and shiny, a necessary condition for a good cyclotron resonance sample. The curvature of one of the sample surfaces was measured using a probe mounted on a travelling microscope stand that had vernier scales for both horizontal and vertical motion. An electrical connection to one side of the sample was connected in series to a resistor, a milliammeter, and a battery. The other terminal of the battery was connected to the probe mounted on the microscope stand. The probe was lowered until a current just started to flow through the circuit, and the height of the probe was read from the vernier scale. Similar readings were taken at one millimeter intervals across the face of the sample. The central part of the sample, a circle 8 mm. in diameter, was found to be raised 0.29 mm. in the center. The curvature was approximately spherical, with a radius of curvature of  $27 \frac{1}{2}$  mm.  $\pm 10\%$ .

Measurements were made at both 35 Gc./sec. and 70 Gc./sec., and the anisotropy of the cyclotron effective mass was plotted for a range of magnetic field directions of  $180^\circ$  in the sample plane. The 35 Gc./sec. sample cavity was constructed so that the bottom half, including the sample, could be rotated about an axis perpendicular to the sample surface. In this way the constant magnetic field was kept perpendicular to the microwave electric field, and in the plane of the sample surface. The 70 Gc./sec. cavity could not be rotated, so that three orientation slots were cut in the sample holder about  $45^\circ$  apart, and the magnet was then turned through  $\pm 45^\circ$  about the perpendicular polarization direction. Separate experiments were performed with the orientation pin in each of the three slots.

The cyclotron effective mass was calculated from the data using a least-squares computer program to fit the best straight line to a plot of  $1/H_n$  versus  $n$  and to calculate  $m_c^* = e/\omega cs$ , where  $s$  is the slope of this line. The program also calculated the phase shift of each set of subharmonics. The values of  $H_n$  used in the program were the values of  $H$  at the derivative-signal maxima, as explained in Chapter II.

Figure 17 shows the cyclotron effective mass results of an experiment at 34.9 Gc./sec. on a mercury crystal which had a sample surface tilted  $4^\circ$  from the trigonal plane. The orientation of the sample surface relative to the trigonal plane is shown in the stereogram of Figure 17 where the dot labelled P gives the position of the pole of the sample surface. The straight lines, ending in the symbol  $\diamond$ , are binary,

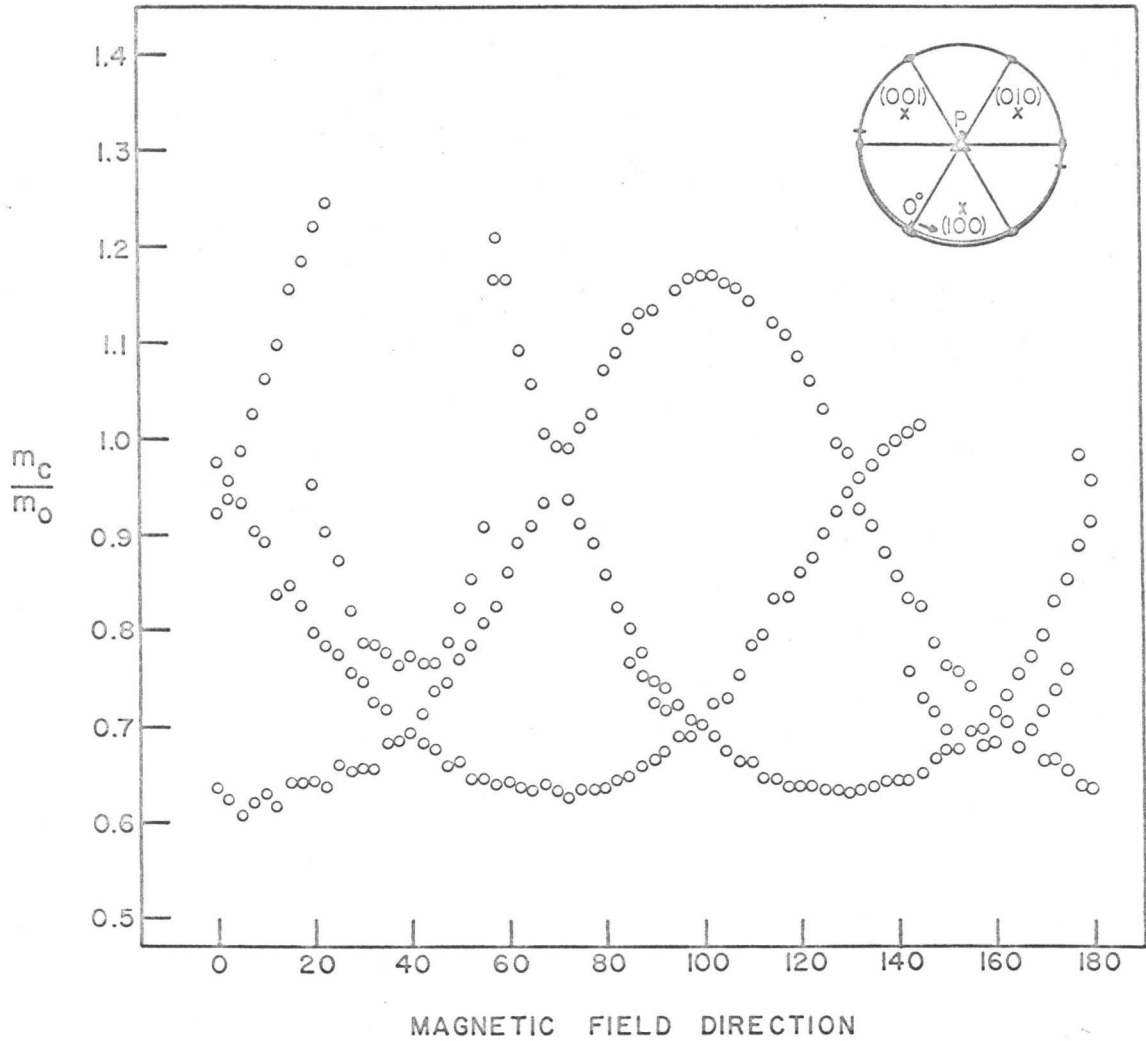


FIGURE 17

CYCLOTRON EFFECTIVE MASS RESULTS FOR A SAMPLE SURFACE  
ORIENTED NEAR THE TRIGONAL PLANE

or two-fold axes. The position of the pole of the sample surface on the stereogram, in latitude and longitude, is  $4^\circ \pm 1^\circ\text{N}$ ,  $1/2^\circ \pm 1^\circ\text{E}$ . The magnetic-field direction labelled  $0^\circ$  on the graph is shown on the stereogram by a short straight line cutting the sample plane, and the direction of rotation of the magnetic field in the sample plane is indicated with an arrow. The possible cyclotron orbits for a magnetic field in the trigonal plane were shown in Figure 8, with the exception of the  $\alpha$ -orbit around the second-zone electron lens. The approximate angular range through which each of these orbits should be observed was calculated using a model based on the band-structure calculations of Keeton and Loucks (1966) (see Figure 33), and is shown in Figure 18. Note that mass curves for the  $\beta$ -,  $\gamma$ -, and  $\mu$ -orbits are centered on bisectrix directions, while those of the  $\delta$ -orbit are centered on binary directions. Cyclotron resonance signals from the electron lenses are possible for any magnetic-field direction, and the signal from a particular lens will indicate a maximum cyclotron effective mass for a magnetic field along the bisectrix direction, and a minimum effective mass for a magnetic field along the binary direction perpendicular to that bisectrix direction. Mass curves A, B, and C of Figure 17 are attributed to electron lenses tilted  $70^\circ$ ,  $66^\circ$ , and  $63^\circ$  respectively from the normal to the sample surface. The curves labelled D, E, and F are visible for an angular range of  $35^\circ$ , and are centered on bisectrix directions. Curve D, which has the largest minimum mass, lies under curve A, which has the largest maximum mass of the three lenses. The Fermi-surface models (nearly-free-electron and relativistic-augmented-

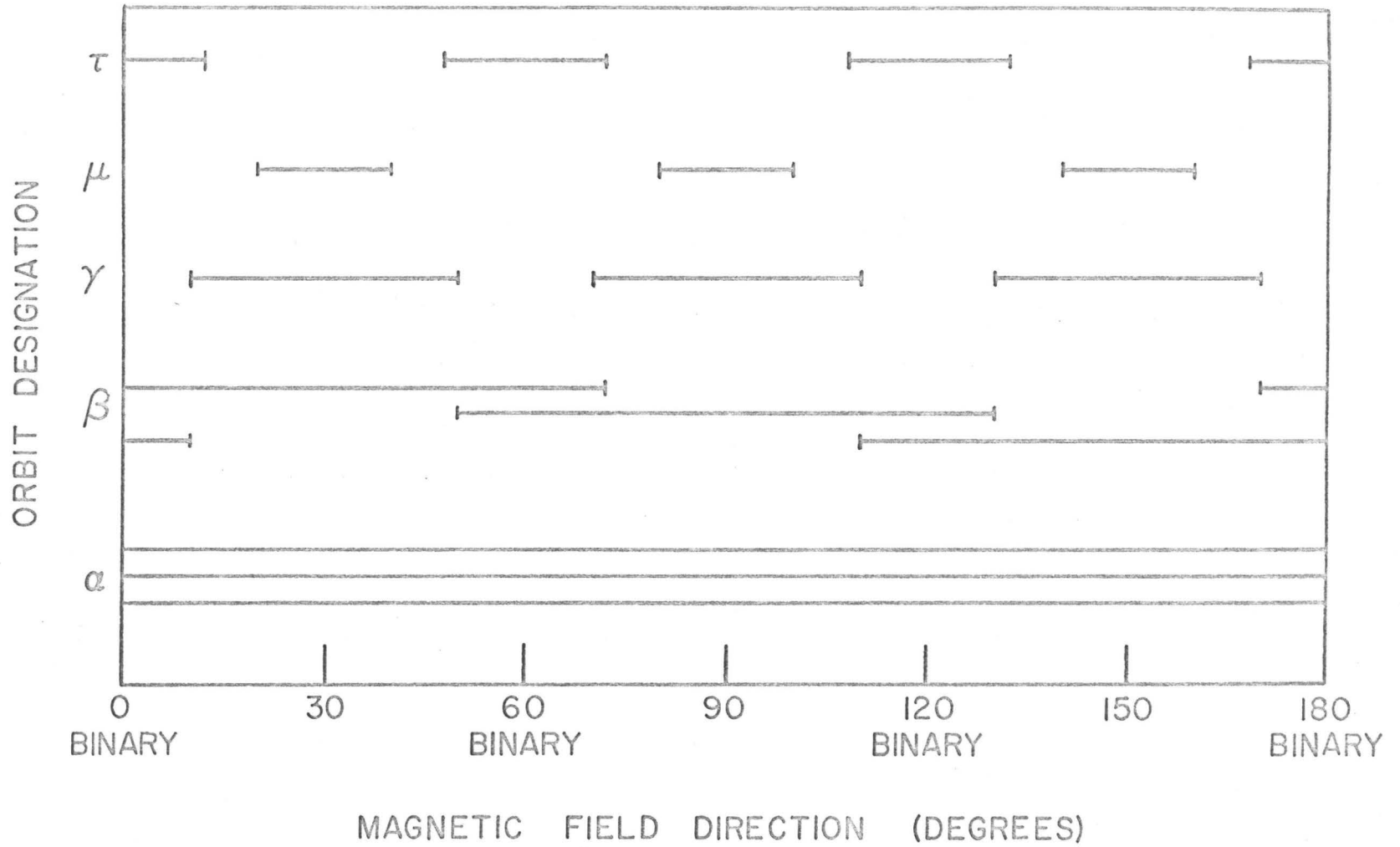


FIGURE 18  
 ANGULAR RANGE OVER WHICH ORBITS REMAIN CLOSED  
 FOR MAGNETIC-FIELD DIRECTIONS IN THE TRIGONAL PLANE

plane-wave) both predict that, for the  $\beta$ - and  $\mu$ -orbits, the curve with the smallest minimum mass should lie under A. For this reason, and because it is visible over almost the same angular range as that predicted for the  $\gamma$ -orbit in Figure 18, D, E, and F are attributed to  $\gamma$ -orbits.

Figure 19 shows the results of an experiment at 69.6 Gc./sec. The sample orientation is shown in the stereogram, where the pole of the sample surface is at  $62\ 1/2^\circ \pm 2^\circ\text{N}$ ,  $36^\circ \pm 2^\circ\text{W}$ . A Laué picture of the sample surface showed a (110) axis and a binary axis each  $25^\circ$  from the normal to the sample surface, and in the same plane as the normal. The long curve of mass values on the right of the diagram corresponds to an electron lens tilted  $70^\circ$  from the normal to the sample surface. The signals on the left of Figure 19 correspond to the other two electron lenses.

Figure 20 shows the cyclotron masses observed in experiments on two samples oriented with two {100} directions in the plane of the sample surface. The pole of the sample surface is at  $42^\circ \pm 2^\circ\text{S}$ ,  $0^\circ \pm 2^\circ\text{W}$ . The two mass curves shown are attributed to second-zone electron lenses (the  $\alpha$ -orbits) by comparison of the results with those shown in Figure 17. These masses were originally attributed to the  $\beta$ -orbits (Dixon and Datars, 1965), when the data of Figure 17 were not available. In this particular sample plane, the minimum mass of the  $\beta$ -orbit is at the same magnetic-field direction as the minimum mass of the lens. The two signals at  $0^\circ$  and  $20^\circ$ , which do not lie on one of the mass curves, are from the third lens, which is almost flat in this sample plane, with a minimum mass in

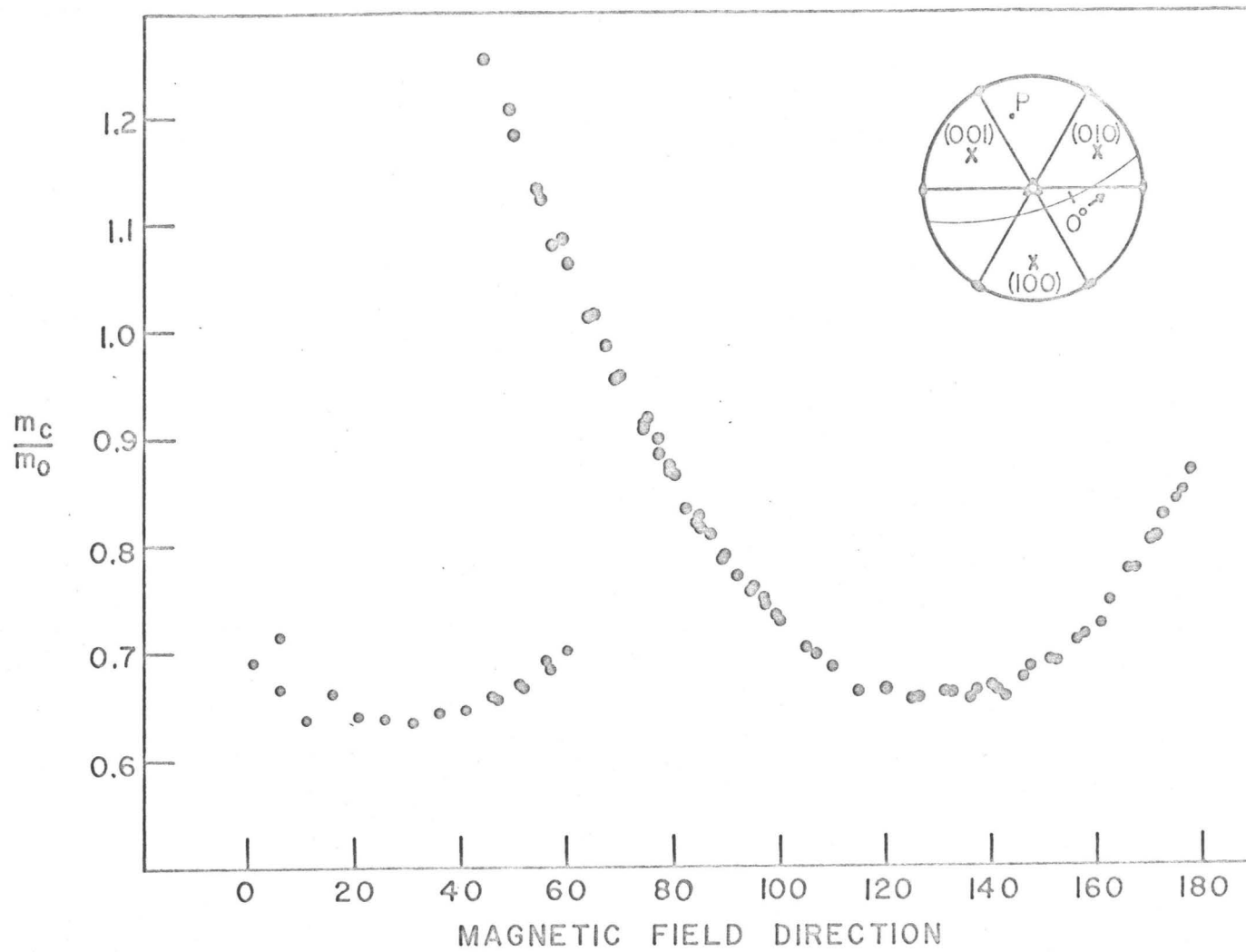


FIGURE 19

CYCLOTRON EFFECTIVE MASS RESULTS AT 69.6 Gc./Sec.

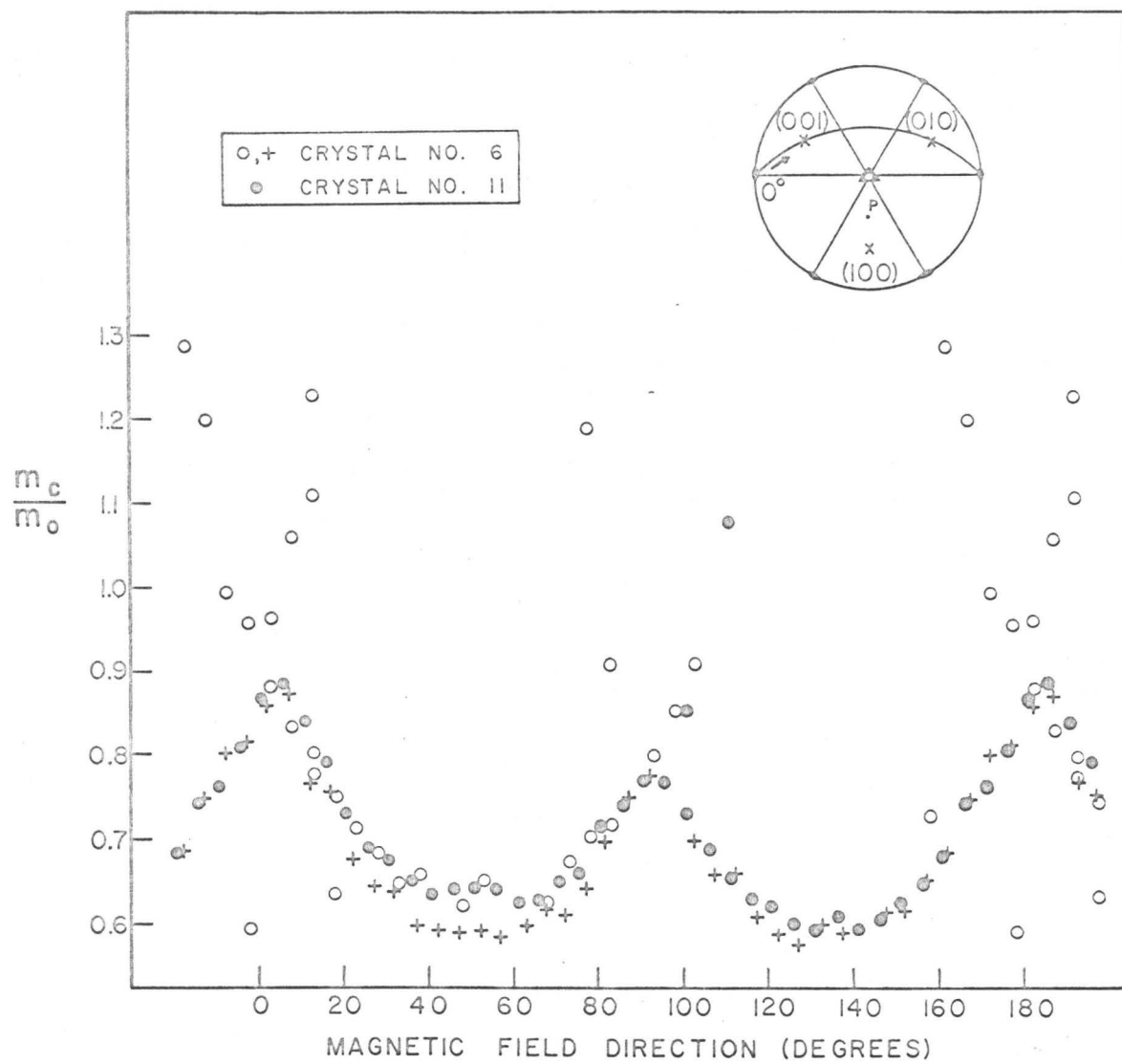


FIGURE 20

CYCLOTRON EFFECTIVE MASS RESULTS  
FROM TWO SIMILARLY-ORIENTED SAMPLES

the binary direction.

The results of an experiment at 34.8 Gc./sec. are shown in Figure 21. The data shown in this Figure, and in Figure 17, were taken with a Varian spectrometer, which has higher sensitivity than the spectrometer used for the data shown in Figures 19 and 20. The sample orientation is shown in the stereogram, with the pole of the sample surface located at  $50^\circ \pm 2^\circ$ S,  $30^\circ \pm 2^\circ$ E. A Laué photograph of the sample surfaces shows a (110) axis tilted  $25^\circ$  from the normal to the sample surface, and a (100) axis tilted  $24^\circ$  from the normal. A plane drawn through the (110) and (100) axes passes  $3^\circ$  away from the normal to the sample surface. The mass curve labelled A is attributed to an electron lens tilted  $83^\circ$  from the normal to the sample surface. The curve labelled B is assigned to a second lens, tilted  $70^\circ$  from the normal to the sample surface. The scattered points labelled C are in the position for resonance signals from the third electron lens. The curve D is attributed to a  $\gamma$ -orbit, since it occurs for a range of magnetic-field directions for which a  $\gamma$ -orbit is possible, and has a minimum-mass value close to that of the  $\gamma$ -orbit in Figure 17. The mass curve labelled E lies directly under the minimum of curve B, and has approximately the same shape as curve B. Because de Haas - van Alphen measurements (Brandt and Rayne, 1966) have indicated an effective mass of 0.18 for the  $\beta$ -orbits, it is tempting to attribute these masses to a  $\beta$ -orbit. They do not have the anisotropy of the  $\beta$ -orbit, however, since the piece of Fermi surface giving rise to that orbit is approximately cylindrical, and should give rise to a mass curve that is curved upwards

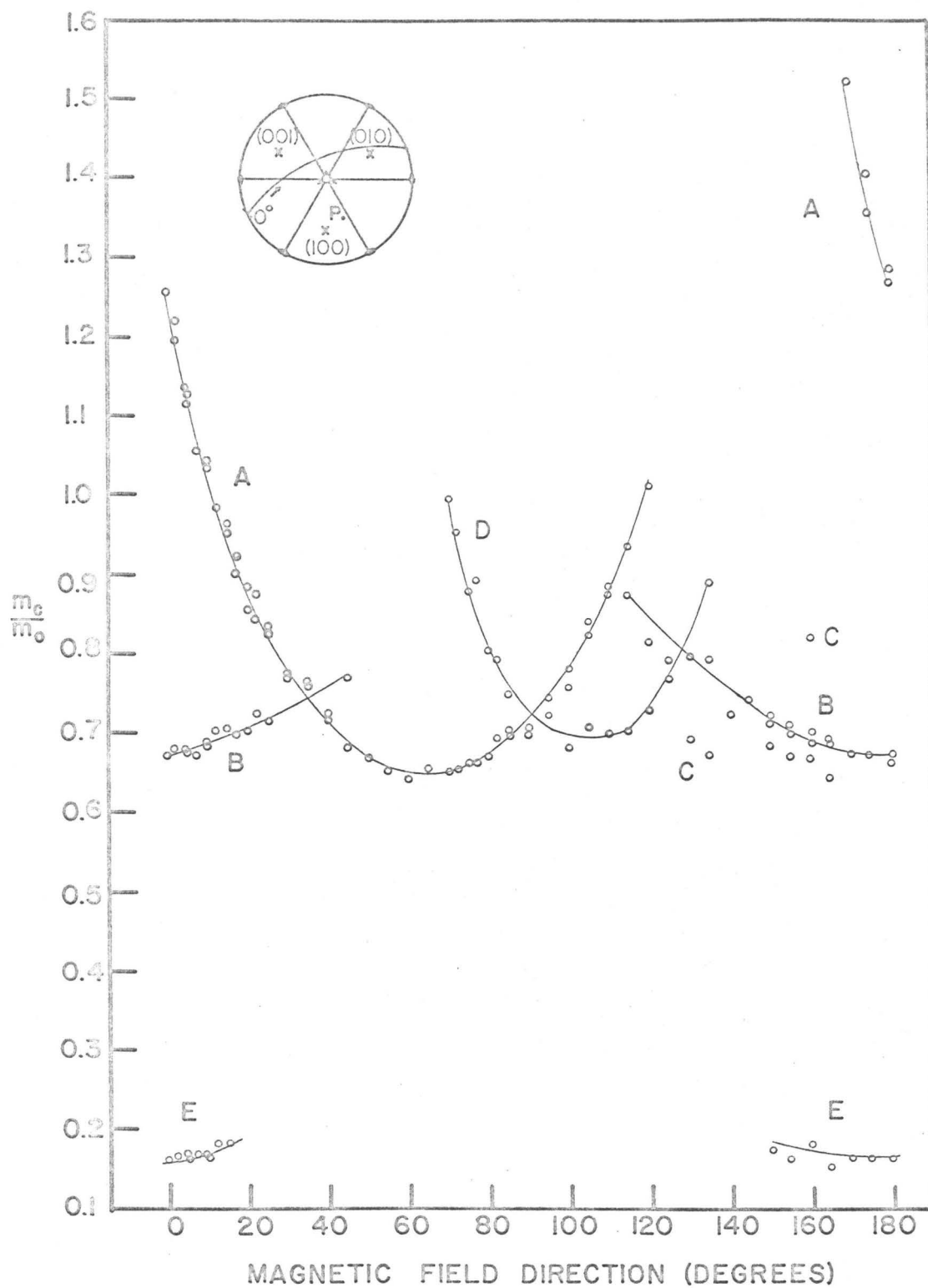


FIGURE 21

CYCLOTRON EFFECTIVE MASS RESULTS FROM A SAMPLE  
ORIENTED AS SHOWN IN THE STEREOGRAM

more than that of the masses labelled E. The curve does not match the anisotropy of any part of the first-zone hole surface. Because it lies directly under the minimum of B, and has approximately the same shape, curve E is possibly due to the same group of electrons as curve B, the electrons of the second-zone lens.

Several traces were taken with the constant magnetic field parallel to the microwave electric field, the parallel-polarization position. In each case only one large set of resonances was observed, which was due to the electron lens. The magnetic-field directions at which parallel-polarization experiments were carried out included directions in which masses of curve E were observed in the perpendicular-polarization position.

#### B. Magnetoresistance Results

Magnetoresistance measurements were made on a single crystal that was originally the long starter tube of one of the cyclotron-resonance samples. Measurements of the voltage across the sample were made for many directions of the D.C. magnetic field, covering an angular range of  $180^\circ$ . A transverse-magnetoresistance rotation curve is shown in Figure 22. The two sharp minima correspond to primary open orbits along  $\{100\}$  directions, and the small minimum on the right side corresponds to a secondary orbit along the binary direction.

Measurements were also made with the sample tilted away from the transverse-magnetoresistance position. In this case the magnetoresistance can be expressed as a sum of two mutually-perpendicular components, one along

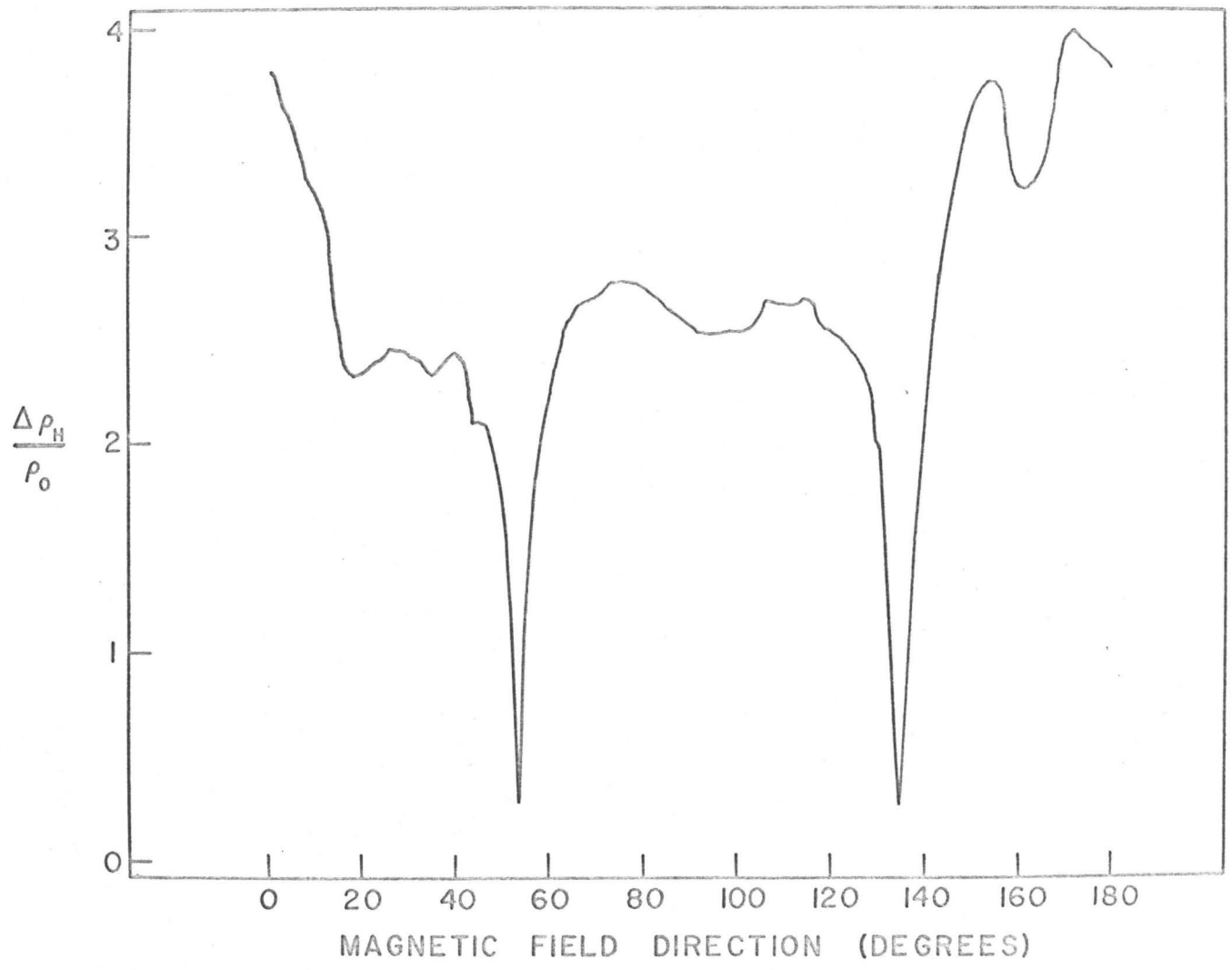


FIGURE 22

TRANSVERSE MAGNETORESISTANCE ROTATION DIAGRAM

the magnetic-field direction, and one perpendicular to it. The component along the magnetic-field direction, the longitudinal magnetoresistance, saturates, while the component perpendicular to the magnetic-field direction, the transverse magnetoresistance, is proportional to  $H^2$  unless there is an open orbit perpendicular to the magnetic field direction, when it saturates. Magnetoresistance rotation plots taken with the sample tilted are shown in Figure 23.

Figure 24 shows a stereographic projection on which the planes corresponding to the faces of the first Brillouin zone are shown, along with the poles of these planes. The diagram is a projection on the trigonal plane, so that plane is represented by the outer circle, and its pole is at the center of the diagram. Planes representing the X-faces are shown by dotted lines, the solid curves represent the L-faces. If there are open orbits in reciprocal space along directions perpendicular to these faces, then corresponding magnetoresistance minima will lie on the curves representing these faces in Figure 24.

The results of many measurements of the type shown in Figure 23 are plotted in Figure 25, where each dot represents a magnetic-field direction at which a resistance minimum was observed. The data are projected on the trigonal plane; the area inside the small circle is a region in which no measurements were made because the sample could not be tilted far enough to include that area. The current direction, which is the axis of the cylindrical sample, is labelled J.

Two curves of minima fall on curves which correspond to the

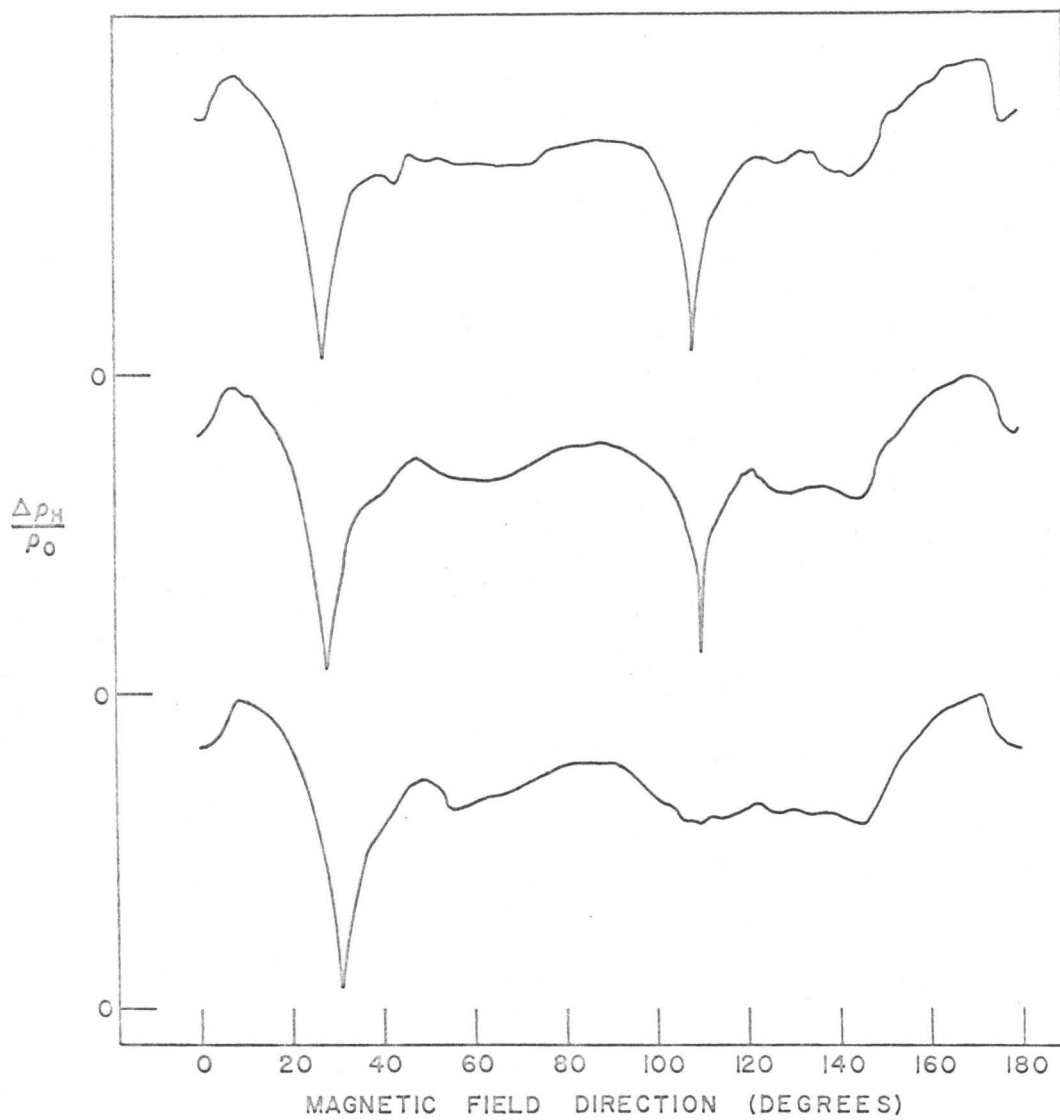


FIGURE 23

MAGNETORESISTANCE ROTATION DIAGRAMS FOR A SAMPLE

TILTED AT THREE DIFFERENT ANGLES

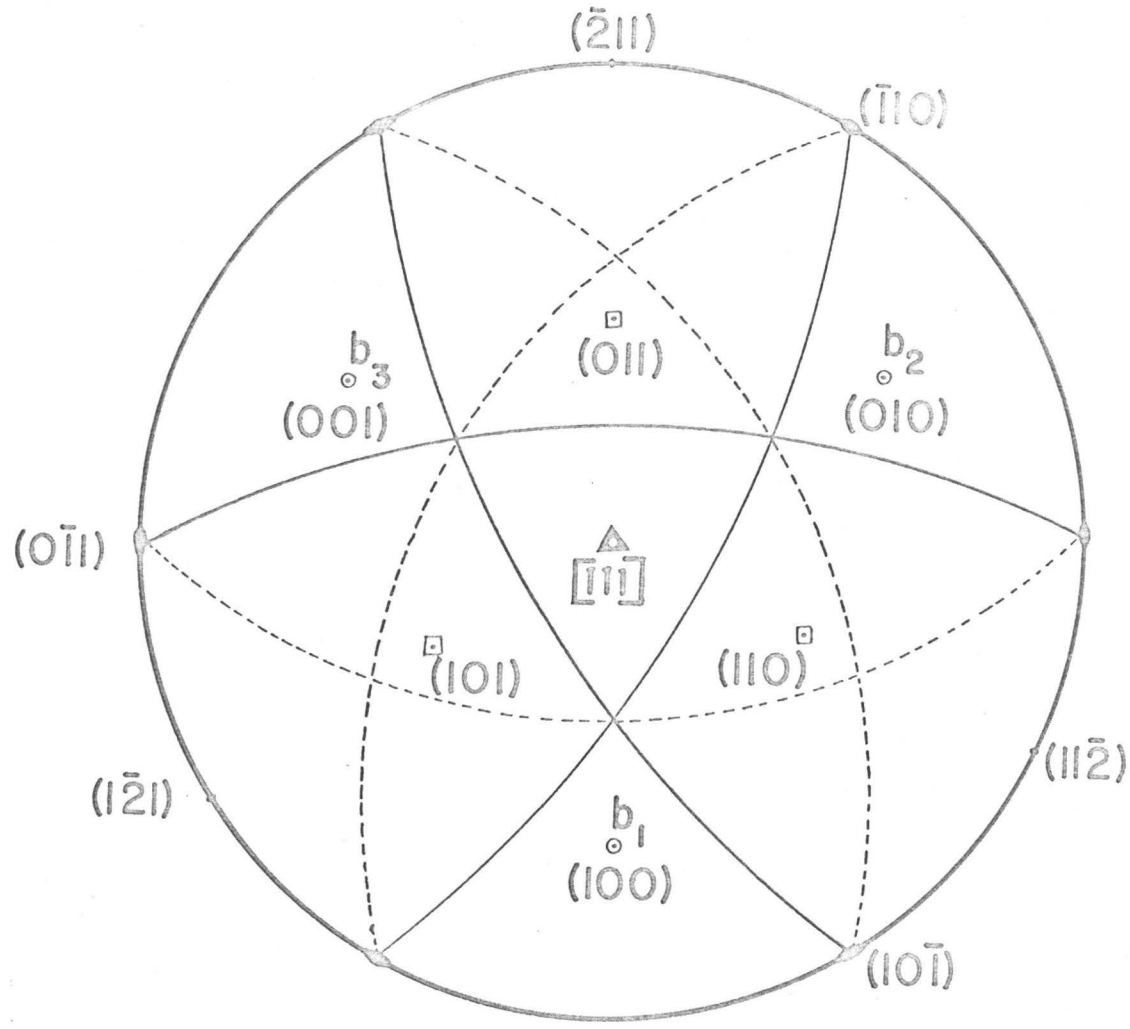


FIGURE 24

STEREOGRAPHIC PROJECTION SHOWING THE PLANES  
 CORRESPONDING TO THE FACES OF THE FIRST BRILLOUIN ZONE

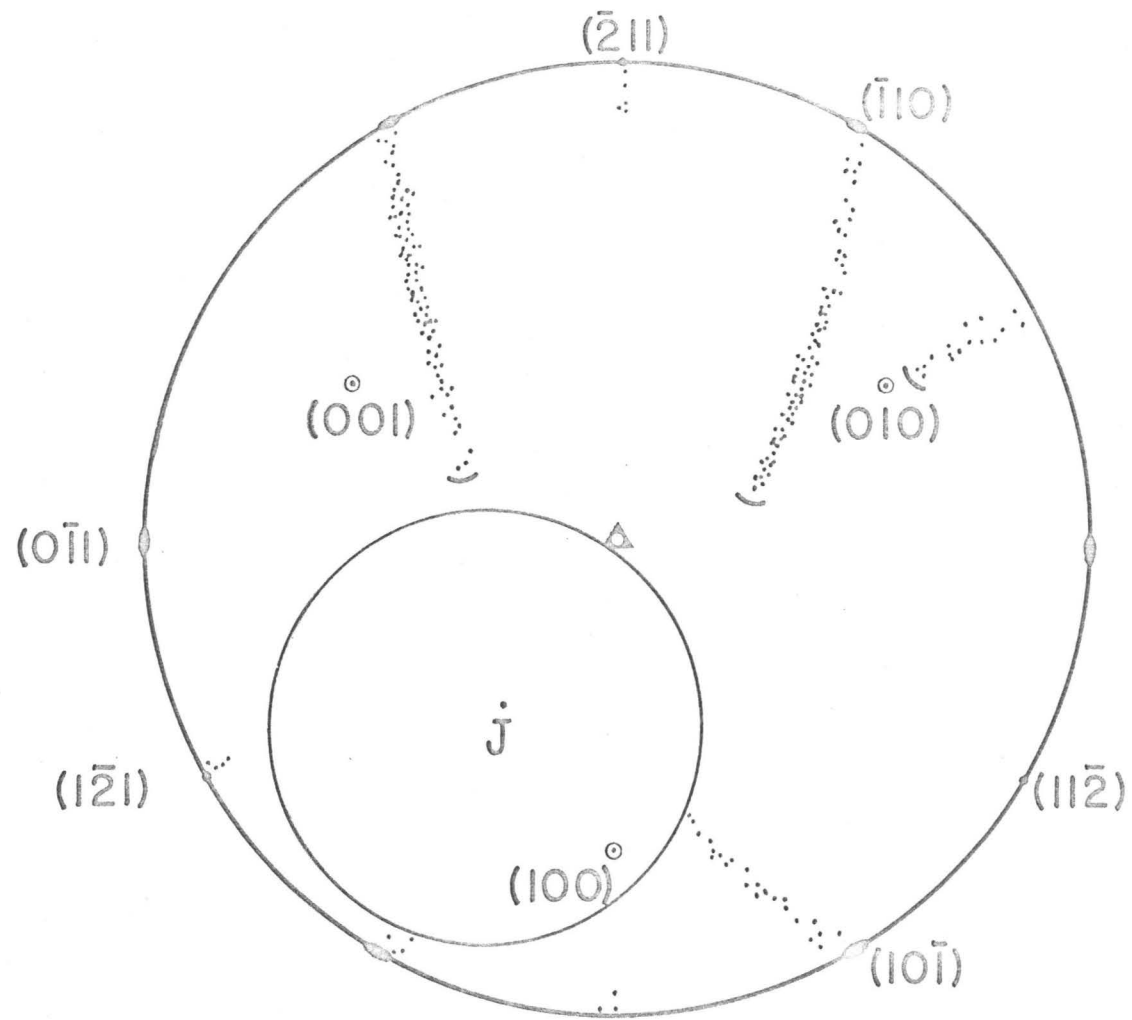


FIGURE 25

MAGNETORESISTANCE RESULTS PROJECTED ON THE TRIGONAL PLANE

curves representing the L-faces in Figure 24. These correspond to primary open orbits along the (010) and (001) directions. The third open orbit, along the (100) direction, did not give magnetoresistance minima because the (100) direction was only  $36^\circ$  from the current direction. A sudden disappearance of magnetoresistance minima is shown by a bracket on the diagram. The magnetoresistance minima corresponding to a particular open orbit disappear when it is no longer possible for an electron, which travels a distance greater than the length of a reciprocal-lattice vector in the open-orbit direction, to stay on the Fermi surface, and also on a plane perpendicular to the magnetic-field direction. The disappearance of the (001) orbit is shown in Figure 23, where the magnetoresistance minimum corresponding to this orbit disappeared as the sample was tilted in the magnetic field. The sample was tilted  $7^\circ$  between each of the measurements shown, but because of the many measurements taken, the cutoff region is known to within two degrees.

Other regions of magnetoresistance minima are shown near the bisectrix directions, and correspond to a secondary open orbit along the binary direction. A sudden disappearance of magnetoresistance minima was observed  $5^\circ \pm 2^\circ$  from the (010) direction. This particular set of minima was more pronounced than the others from secondary orbits because it corresponded to an open-orbit direction  $73^\circ$  from the current direction.

Figure 26 shows the dependence of the magnetoresistance on magnetic-field strength. The bottom curve corresponds to a magnetic-field direction aligned accurately at the magnetoresistance minimum of a primary

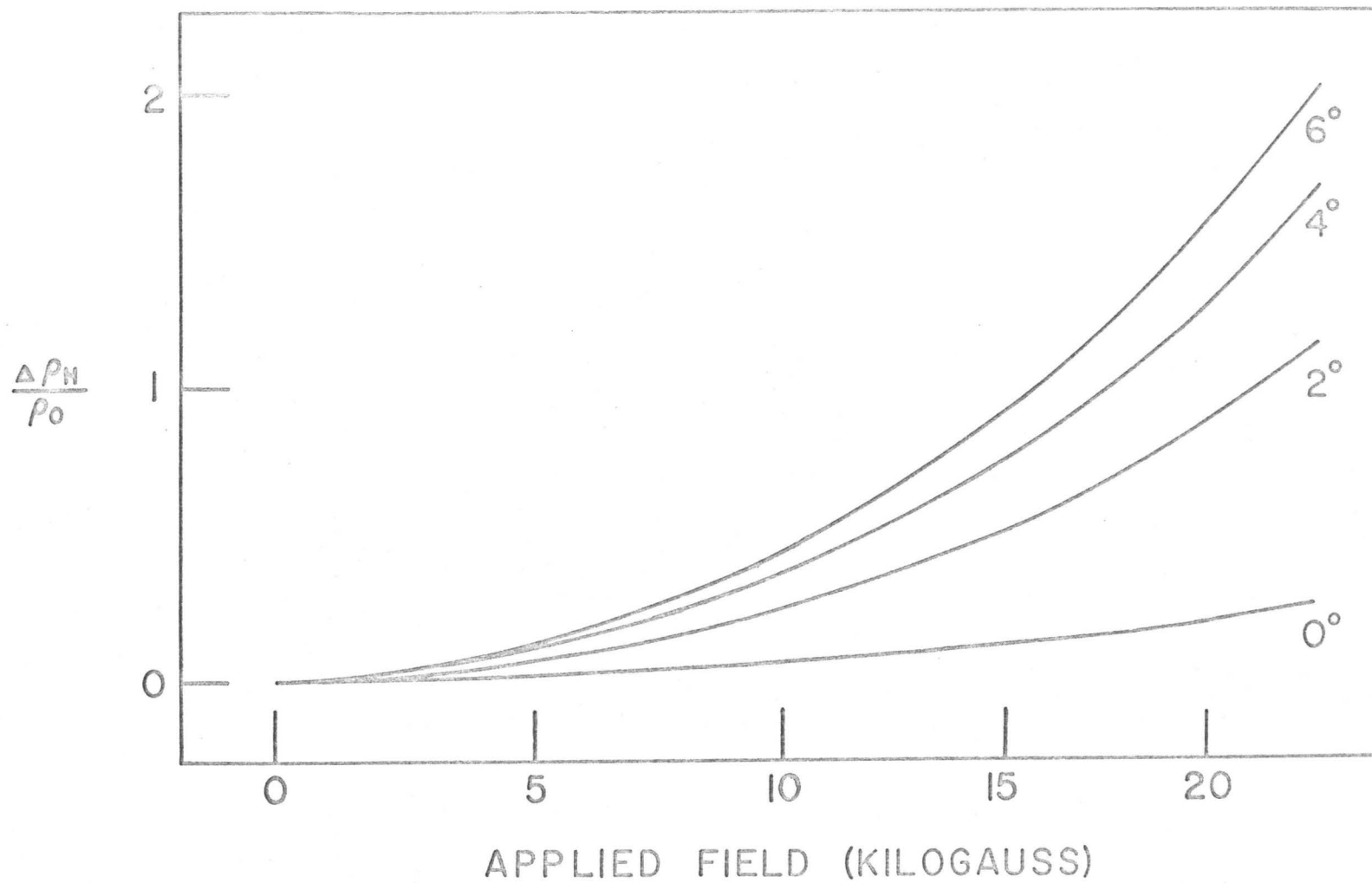


FIGURE 26

DEPENDENCE OF THE MAGNETORESISTANCE ON MAGNETIC-FIELD STRENGTH

orbit. The other curves correspond to magnetic-field directions set at  $2^\circ$  intervals away from the minimum value. The quadratic dependence of the magnetoresistance is evident even in the lower curve, and better alignment of the magnetic field perpendicular to the open orbit direction did not cause the quadratic dependence to disappear. When the current direction was set perpendicular to the magnetic-field direction, measurements showed that  $\nabla \rho_{xx} / \rho_0 \propto H^A$ , where A varied from 1.95 to 2.04, confirming that mercury is a compensated metal. No oscillatory behaviour of the DC magnetoresistance corresponding to the Shubnikov - de Haas effect has been observed up to twenty-three kilogauss.

### C. Quantum Oscillations of the Microwave Surface Impedance

Oscillations of the microwave surface impedance for magnetic field strengths above ten kilogauss have been observed during cyclotron resonance experiments at  $1.22^\circ\text{K}$ . Examples of these oscillations are shown in Figure 27. The top curve is the best one obtained, and shows beating of two frequencies near a cross-over point of the data in Figure 28. The bottom curve is typical of the results obtained from this sample (cyclotron resonance results for this sample are shown in Figure 17). The oscillations are periodic in  $1/H$ , and if analyzed as cyclotron resonance subharmonics yield an effective mass much larger than would be expected in mercury. If the oscillations are analyzed in the same way as de Haas - van Alphen oscillations, they yield results identical in both frequency and anisotropy to de Haas - van Alphen results from the  $\beta$ -orbits (Brandt and Rayne, 1966). For this reason, the oscillations are identified as quantum oscillations of

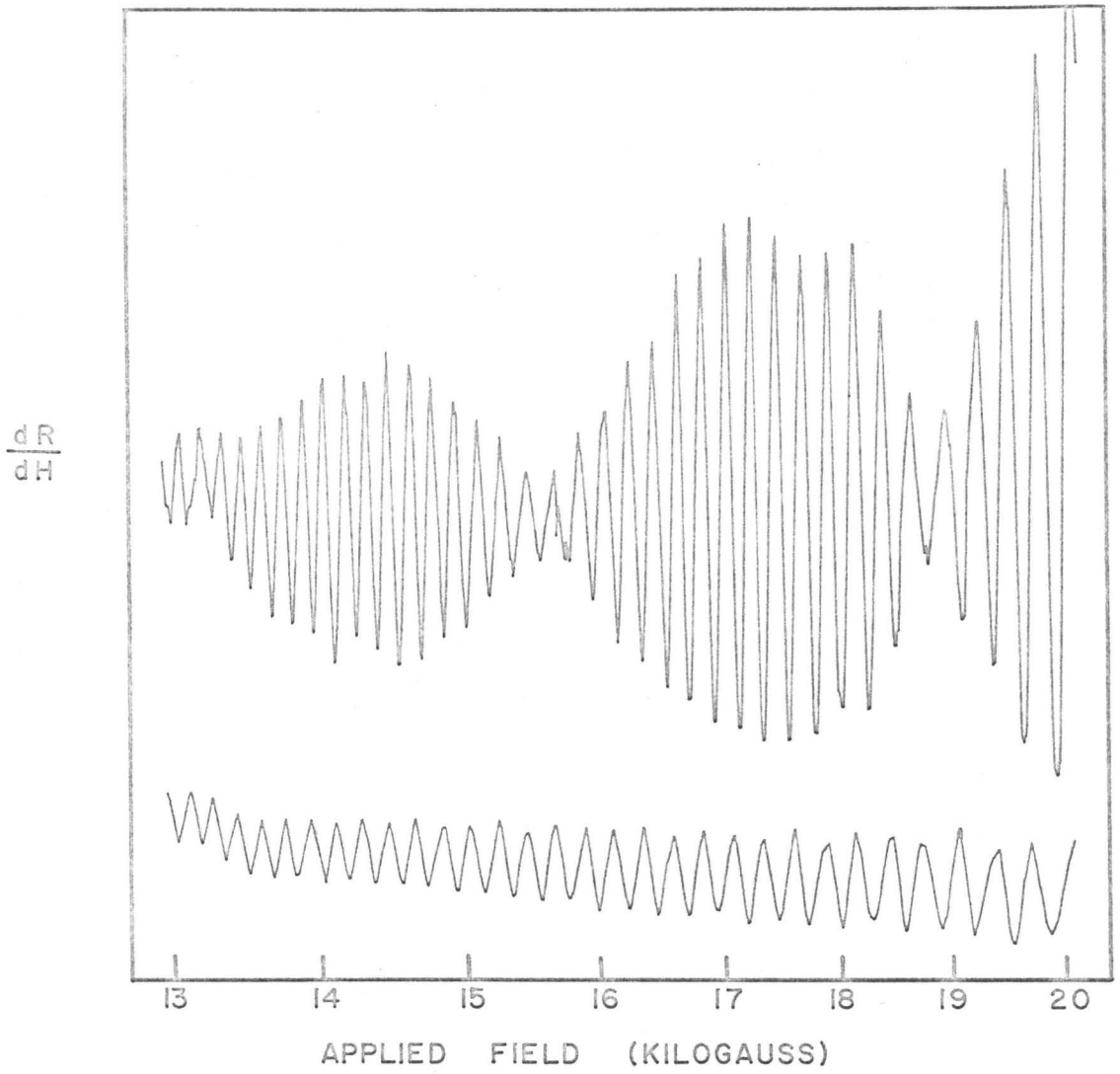


FIGURE 27

OSCILLATIONS OF THE MICROWAVE SURFACE IMPEDANCE

the microwave surface impedance. A plot of the frequencies observed is shown in Figure 28, where the sample orientation is the same as that for the cyclotron resonance results in Figure 17. Note that the angular range over which each branch is observed is just a little smaller than that predicted for the  $\beta$ -orbit in Figure 18, and larger than the angular range of either the  $\gamma$ - or  $\mu$ -orbits, which are also centered on bisectrix axes. In Figure 28, the two data points at the top left of the diagram are part of the data curve on the right, and two of the data points at top right are part of the data curve on the left. No frequencies corresponding to any other orbit have been observed.

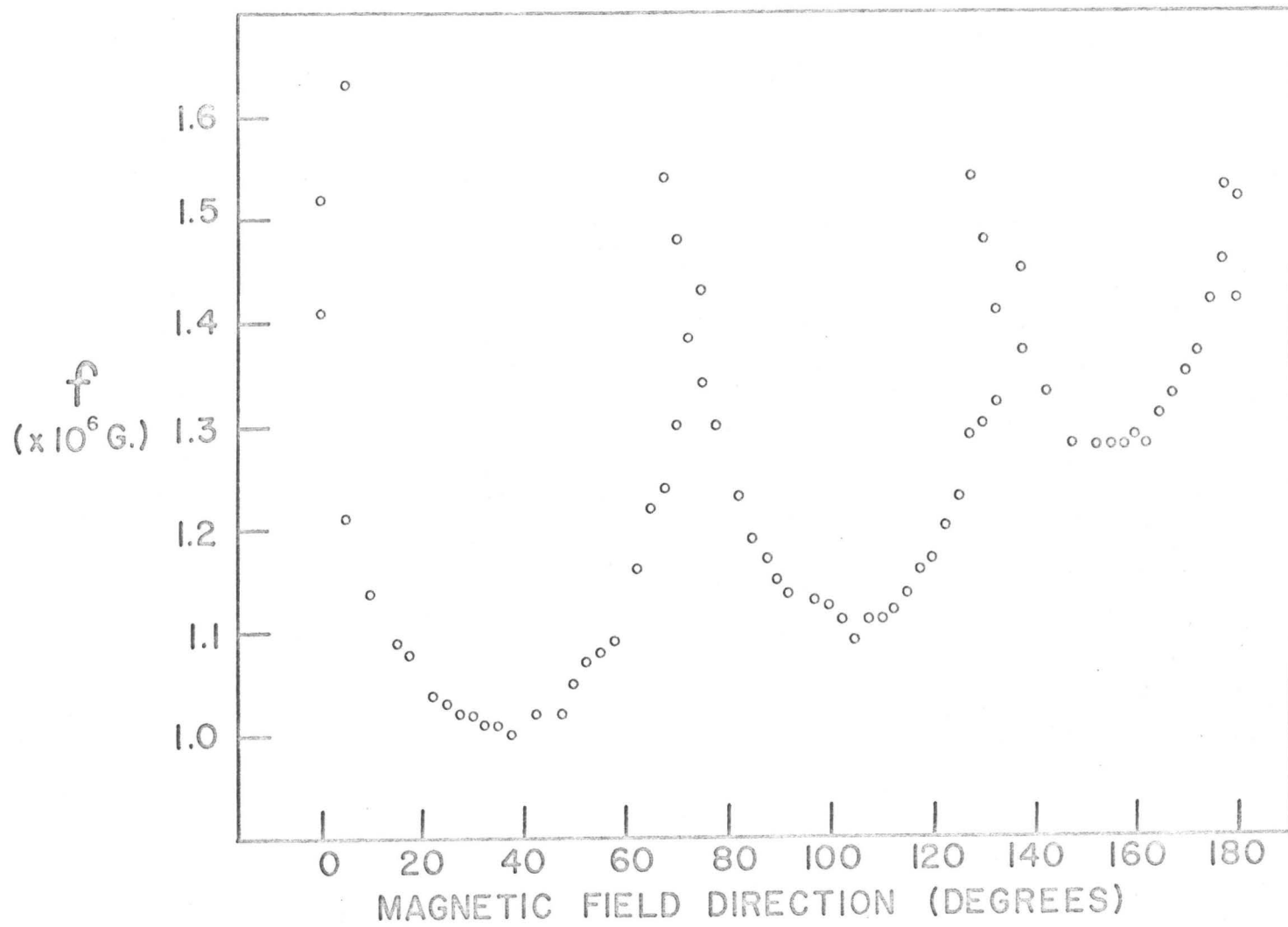


FIGURE 28  
 SURFACE IMPEDANCE OSCILLATION FREQUENCIES OBSERVED IN THE SAMPLE  
 WHOSE ORIENTATION IS SHOWN IN FIGURE 17

## CHAPTER VI

DISCUSSION OF EXPERIMENTAL RESULTSA. An Ellipsoidal Fit to the Cyclotron Resonance Data

A least-squares fit has been made to the data from one of the second-zone electron lenses, to compare the lens to an ellipsoid of revolution. If a set of experimental variables  $F_i$  are measured, in terms of two variables  $f_{1i}$  and  $f_{2i}$ , then we can write:

$$F_i = Af_{1i} + Bf_{2i} . \quad (\text{VI-1})$$

The difference between the experimentally-measured quantity and the equivalent point on the fitted curve is given by

$$d_i = Af_{1i} + Bf_{2i} - F_i ,$$

$$\text{and } \sum_i d_i^2 = \sum_i (Af_{1i} + Bf_{2i} - F_i)^2 .$$

The method of least squares requires that

$$\frac{\partial (\sum_i d_i^2)}{\partial A} = \frac{\partial (\sum_i d_i^2)}{\partial B} = 0 .$$

Using (VI-1), this means that

$$A \sum_i f_{1i}^2 + B \sum_i f_{2i} f_{1i} - \sum_i F_i f_{1i} = 0 \quad (\text{VI-2})$$

$$\text{and } B \sum_i f_{2i}^2 + A \sum_i f_{1i} f_{2i} - \sum_i F_i f_{2i} = 0 . \quad (\text{VI-3})$$

By defining

$$x = \sum_i f_{1i}^2,$$

$$y = \sum_i f_{2i}^2,$$

$$z = \sum_i f_{1i} f_{2i},$$

$$w = \sum_i F_i f_{1i},$$

$$g = \sum_i F_i f_{2i},$$

(VI-2) and (VI-3) can be written:

$$\left. \begin{aligned} Ax + Bz - w &= 0, \\ Az + By - g &= 0. \end{aligned} \right) \quad (\text{VI-4})$$

Equation (VI-4) can be solved for the unknown quantities A and B.

Equation (II-9) for the cyclotron effective mass of an ellipsoid can be written in terms of the variables  $\sin^2 \theta_i$  and  $\cos^2 \theta_i$

$$\frac{1}{m_i} = \frac{1}{m_2 m_3} \sin^2 \theta_i + \left( \frac{\cos^2 K}{m_1 m_3} + \frac{\sin^2 K}{m_1 m_2} \right) \cos^2 \theta_i, \quad (\text{VI-5})$$

where K is the angle between the major axis of the ellipsoid and the normal to the sample surface, and  $\theta$  is the rotation angle in the plane of the sample surface. For an ellipsoid of revolution,  $m_1 = m_2$ , and (VI-5) becomes:

$$\frac{1}{m_i} = \frac{1}{m_1 m_3} \sin^2 \theta_i + \left( \frac{\cos^2 K}{m_1 m_3} + \frac{\sin^2 K}{m_1} \right) \cos^2 \theta_i. \quad (\text{VI-6})$$

The definitions of A and B are obtained by comparing (VI-6) and (VI-1). A card listing of the computer program, written for the McMaster IBM 7040 computer, is shown in Table 2.

An ellipsoidal fit was made to the data curve labelled B in Figure 20, and the results of this calculation were compared with the data from other second-zone electron lenses. The lens of curve B was tilted  $66^\circ \pm 1^\circ$  from the normal to the sample surface. The parameters of the ellipsoid of revolution that best fit the data were  $m_1 = m_2 = 0.219 m_0$ ,  $m_3 = 1.34 m_0$ . This ellipsoid was then used to fit lens A (tilt angle  $70^\circ \pm 1^\circ$ ) and lens C (tilt angle  $63^\circ \pm 1^\circ$ ). The results of these comparisons are shown in Figure 29. The best fit for lens C was for a tilt angle of  $62^\circ$ ; this is the comparison shown in Figure 29. Figure 30 shows the results of a comparison of the computed ellipsoid with a lens tilted  $70^\circ$  from the normal to the sample surface. Note that in each case the calculation predicts a maximum mass that is too large, and a minimum mass that is too small. An attempt to compare an ellipsoid with the parameters calculated above with the data from the lens tilted  $20^\circ$  from the normal to the sample surface (data curve B) in Figure 21 was not successful. The comparison fell below the measured masses for all magnetic-field directions. A measurement of the effective mass for all magnetic-field directions around a lens with a tilt angle of  $0^\circ$  would be useful to show how far the lens differed from an ellipsoid of revolution. The latter would give a constant effective mass for a lens having this orientation.

#### B. A Cylindrical Fit to the Quantum Oscillation Data

The cross-sectional area of a cylinder at an angle  $\theta$  from the

Table 2

```

C   LEAST SQUARES FIT TO ELLIPSOID OF REVOLUTION
    DIMENSION CM(36), CM5(36), THETA(36), ST2(36), CT2(36)
1  FORMAT (9F6.3)
2  FORMAT (18F6.3/18F6.3//)
6  FORMAT (1F6.1)
5  READ (5,6) TILT
    WRITE (6,6) TILT
    READ (5,1) (CM(I), I = 1,36)
    WRITE (6,2) (CM(I), I=1,36)
    TILTR = TILT*3.1415927/180.0
    X=0.0
    Y=0.0
    Z=0.0
    W=0.0
    G=0.0
    DO 3 I=1,36
      THETA(I) = FLOAT(5*I-5)*3.1415927/180.0
      ST2(I) = (SIN(THETA(I)))**2
      CT2(I) = (COS(THETA(I)))**2
      X=X+ST2(I)**2
      Y=Y+CT2(I)**2
      Z=Z+CT2(I)*ST2(I)
      CM5(I)=CM(I)**(-2)
      W=W+CM5(I)*ST2(I)
3  G=G+CM5(I)*CT2(I)
      B=(G-W*Z/X)/(Y-(Z**2)/X)
      A=(W-B*Z)/X
      CM1=SQRT((SIN(TILTR))**2/(B-A*(COS(TILTR))**2))
      CM3=(A*CM1)**(-1)
4  FORMAT (2F6.3)
    WRITE (6,4) CM1, CM3
    CM2=CM1
    CM4=CM1*CM2*CM3
    DO 7 J=1,91
      TILT1 = J-1
      TILT1R = TILT1*3.1415927/180.0
      X2 = (SIN(TILT1R))**2
      Y2 = (COS(TILT1R))**2
      DIMENSION THETA1(19), CMASS(19), A1(19), B1(19)
      DO 8 I = 1,19
        THETA1(I) = FLOAT(I-1)*3.1415927/36.0
        A1(I) = (SIN(THETA1(I)))**2
        B1(I) = (COS(THETA1(I)))**2
8  CMASS(I) = SQRT(CM4/(CM1*A1(I)+CM2*B1(I)*Y2+CM3*B1(I)*X2))
9  FORMAT (8H TILT1= ,F6.1//)
    WRITE (6,9) TILT1
10 FORMAT (9F6.3//10F6.3//)
7  WRITE (6,10) (CMASS(I), I=1,19)
    STOP
    END

```

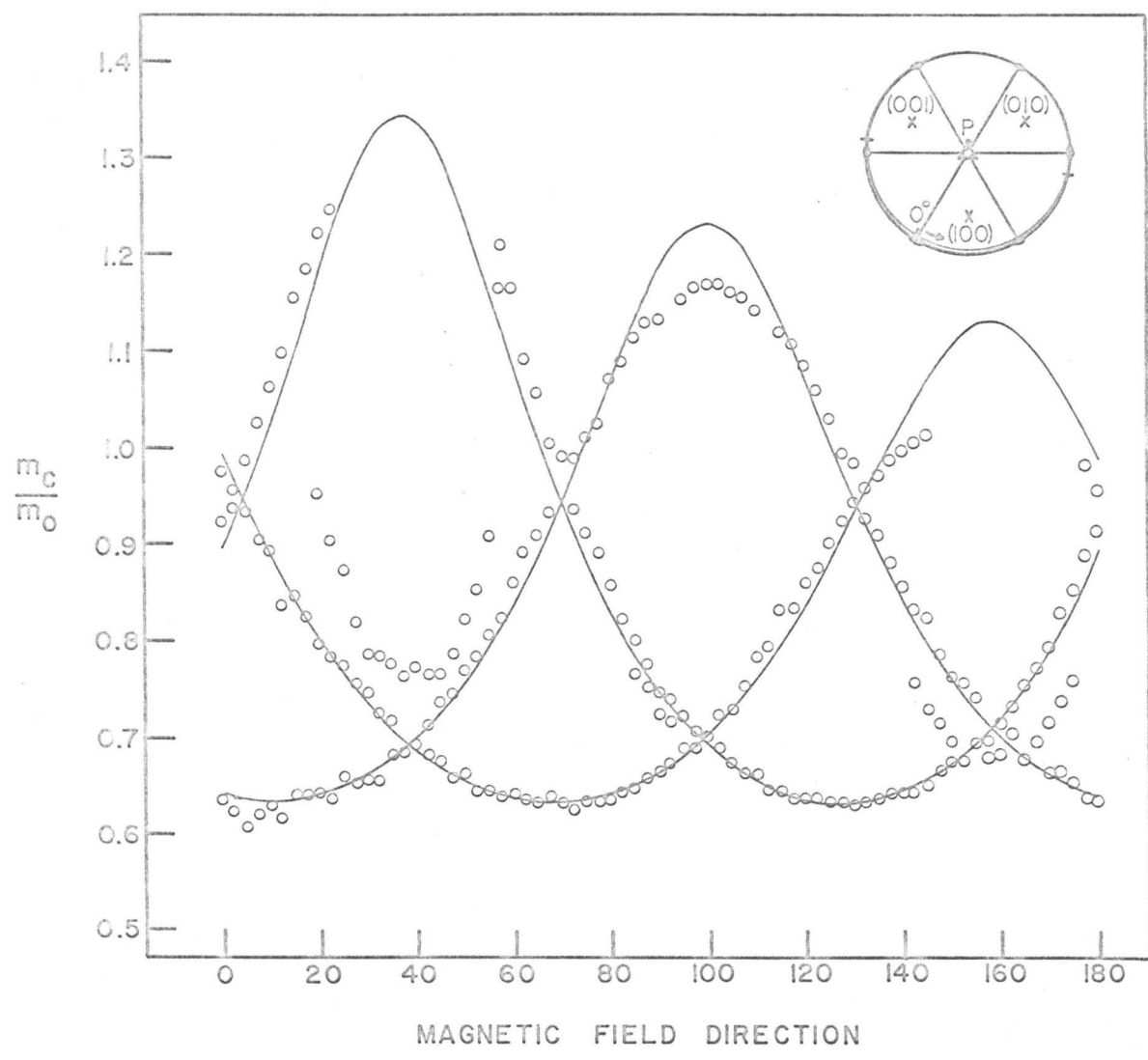


FIGURE 29

ELLIPSOIDAL FITS TO CYCLOTRON MASS DATA FROM THE ELECTRON LENSES

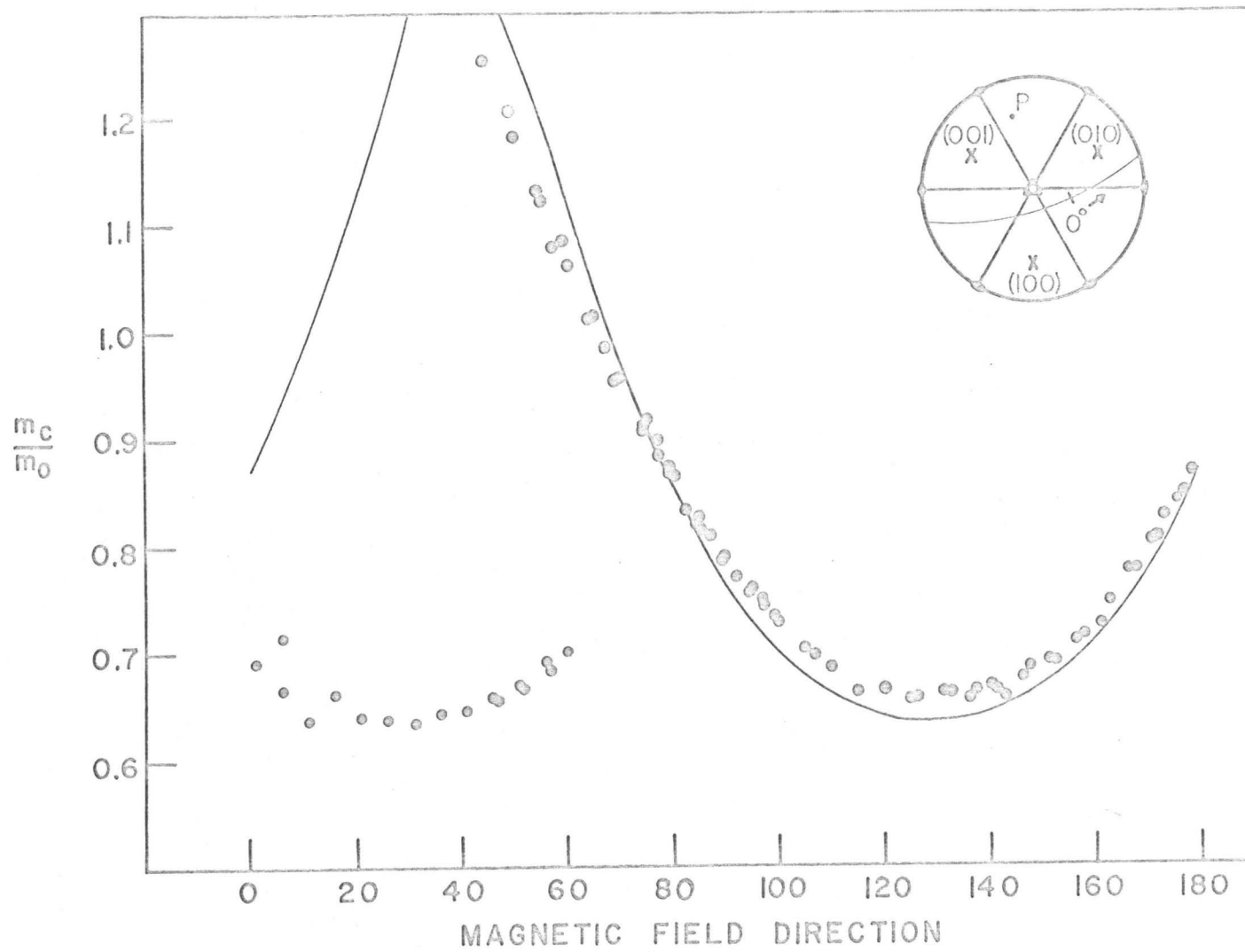


FIGURE 30

AN ELLIPSOIDAL FIT TO THE 4-mm. CYCLOTRON MASS DATA

minimum cross-sectional area in the plane of rotation of the magnetic field direction, is given by

$$A(\theta) = \frac{A_0}{\cos \theta} \quad (\text{VI-7})$$

where  $A_0$  is the minimum area of the cylinder in that plane. Since the frequency of the oscillations is proportional to  $A$  (see equation (II-15)), (VI-7) can be written

$$f(\theta) = \frac{f_0}{\cos \theta}. \quad (\text{VI-8})$$

A cylindrical fit to the quantum oscillation data is shown in Figure 31, where  $f_0$  was taken to be the minimum frequency in each branch. The fitted curve in each case lies outside the experimental curve as  $\theta$  is increased, showing that the cross-sectional area of this orbit is larger than that for a cylinder. The experimental result represents a cylinder that is flared out at the ends where it joins the rest of the Fermi surface. A closed section of the Fermi surface would give a different result. In this case the cross-sectional area of the orbit would not increase as fast as that of a cylinder as the magnetic field was rotated away from the minimum-area position, and the experimental points would lie outside the calculated curve.

### C. Comparison of the Data with the Nearly-Free-Electron Approximation

#### 1. Cyclotron Resonance Data

Of the two cyclotron orbits observed in this experiment ( $\alpha$  and  $\gamma$ ), only the  $\alpha$ -orbit is present in a similar form in the nearly-free-electron

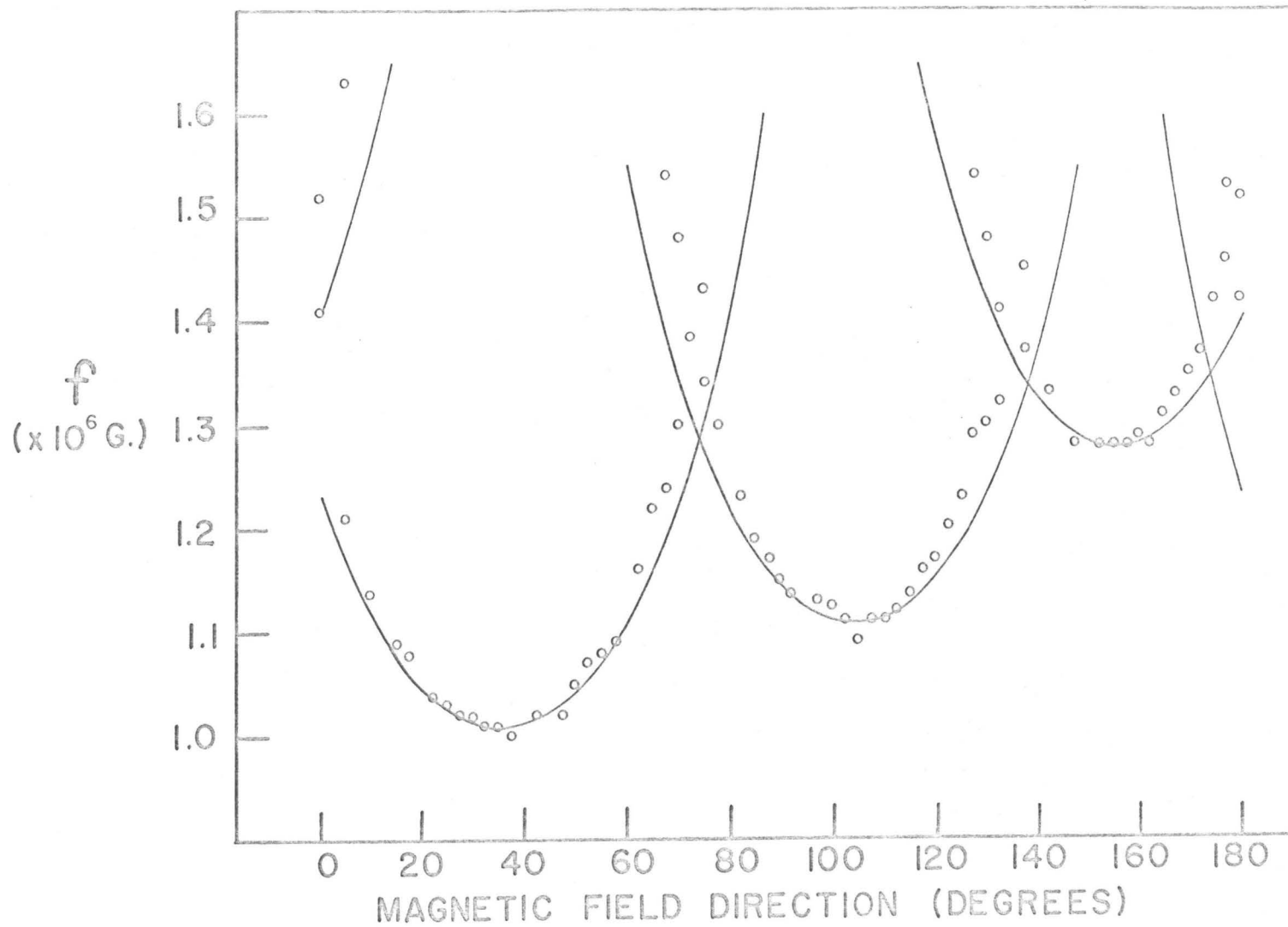


FIGURE 31

CYLINDRICAL FITS TO THE QUANTUM OSCILLATION DATA

approximation. This approximation predicts a minimum effective mass for the  $\alpha$ -orbit (electron lens) of  $0.36 m_0$  and a maximum mass of  $1.0 m_0$ . This experiment has measured a minimum effective mass for the  $\alpha$ -orbit of from  $0.60 m_0$  to  $0.65 m_0$ , depending on the orientation of the lens relative to the sample plane. The maximum mass has not been measured, but it can be estimated from Figure 21 to be about  $1.7 m_0$ . The discrepancy between the measured and predicted values is of the same order of magnitude as that found by Harrison (1960) in aluminum and may be partially due to the fact that electron-electron and electron-phonon interactions are not included in the band-structure mass. The effect of these interactions on the cyclotron effective mass was discussed by Ashcroft (1965), who found that the effect could be quite large.

The  $\gamma$ -orbit, which stretches across the top face of the Brillouin zone in the nearly-free-electron approximation, would be cut in two by the existence of a neck through the T-face. The nearly-free-electron approximation predicts an effective mass of  $0.79 m_0$  for this orbit; this experiment measures an effective mass of  $0.7 m_0$  (see Figure 17), with the magnetic field along a bisectrix direction. Because the nearly-free-electron approximation normally predicts a mass that is lower than that observed, and because the orbit is observed over a larger angular range than would be expected for the nearly-free-electron orbit, these data are taken as evidence of a neck through the T-face.

## 2. Magnetoresistance Data

The magnetoresistance data fits the nearly-free-electron Fermi

surface with only small changes. The nearly-free-electron approximation predicts open orbits along the {100} directions, and along the binary directions. Both orbits are evident in the data. This approximation predicts that the {100}-directed orbits will be visible for all magnetic-field directions in a plane perpendicular to the open-orbit direction, while the data (see Figure 25) indicates that the orbit disappeared for an angular range of  $\pm 26^\circ$  ( $\pm 2^\circ$ ), measured from the projection of the trigonal direction on the plane perpendicular to the orbit direction. For this range of angles it was no longer possible for the electron to stay on the Fermi surface, and at the same time on a plane perpendicular to the magnetic-field direction, for a distance greater than the length of one reciprocal-lattice vector in the open-orbit direction. This indicates that the arms along the X-faces and the cap on the T-faces are thinner than those predicted by the nearly-free-electron approximation. The binary-directed orbit is cut off at a magnetic-field direction  $5^\circ$  ( $\pm 2^\circ$ ) from the (100) direction. The nearly-free-electron model supports this open orbit for a larger range of magnetic-field directions than is indicated in the data, and the absence of this open orbit for a magnetic-field direction along the (100) direction is conclusive proof of a neck through the T-faces. This orbit would be supported by the model for any size neck through the X-faces, as long as no neck existed through the T-faces.

### 3. Quantum Oscillation Data

The data shown in Figure 28 indicates a cross-sectional area for

the  $\beta$ -orbit that is only 1/10 of the area of the same orbit in the nearly-free-electron approximation. This suggests that contact of the Fermi surface at the center of the X-faces has broken the nearly-free-electron arm into two narrow tubes directed along the long dimension of the X-faces. Otherwise, the data has the anisotropy predicted by the nearly-free-electron approximation.

D. Comparison of the Data with the Relativistic-Augmented-Plane-Wave Approximation

The results of a relativistic-augmented-plane-wave calculation (Loucks, 1965) for mercury by Keeton and Loucks (1966) are shown in Figure 32. The intersection of the Fermi surface with the Brillouin-zone faces is shown in Figure 33, where all the symmetry points are shown except  $\Gamma$ , the center point of the Brillouin zone. This approximation predicts that the Fermi surface will touch both the X- and T-faces, and was used to estimate the angular range through which the various cyclotron orbits remained closed (see Figure 18). The cyclotron-resonance results for the  $\gamma$ -orbit, and the quantum-oscillation results for the  $\beta$ -orbit, fitted these predictions very well. The mass curve labelled E in Figure 21 does not have the anisotropy of any part of the Fermi surface predicted by this approximation, however, and the origin of these masses cannot be explained at this time. The model requires only one small change to agree with the magnetoresistance data. The calculated results of Figure 33 support an open orbit along the binary direction, with the magnetic field aligned along the (100) direction, and the data of Figure 25 indicated that

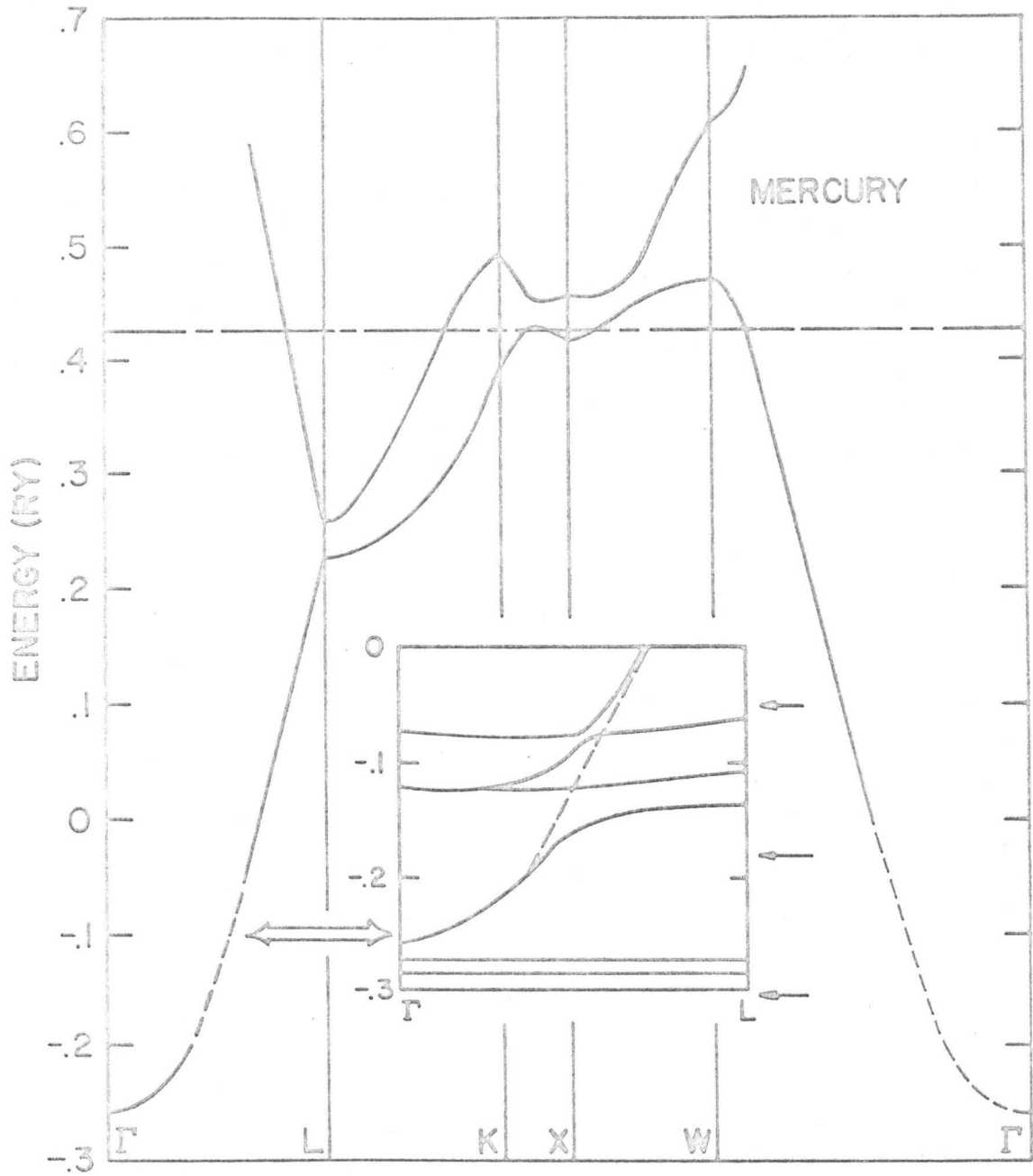


FIGURE 32

BAND STRUCTURE RESULTS FROM  
RELATIVISTIC-AUGMENTED-PLANE-WAVE CALCULATION

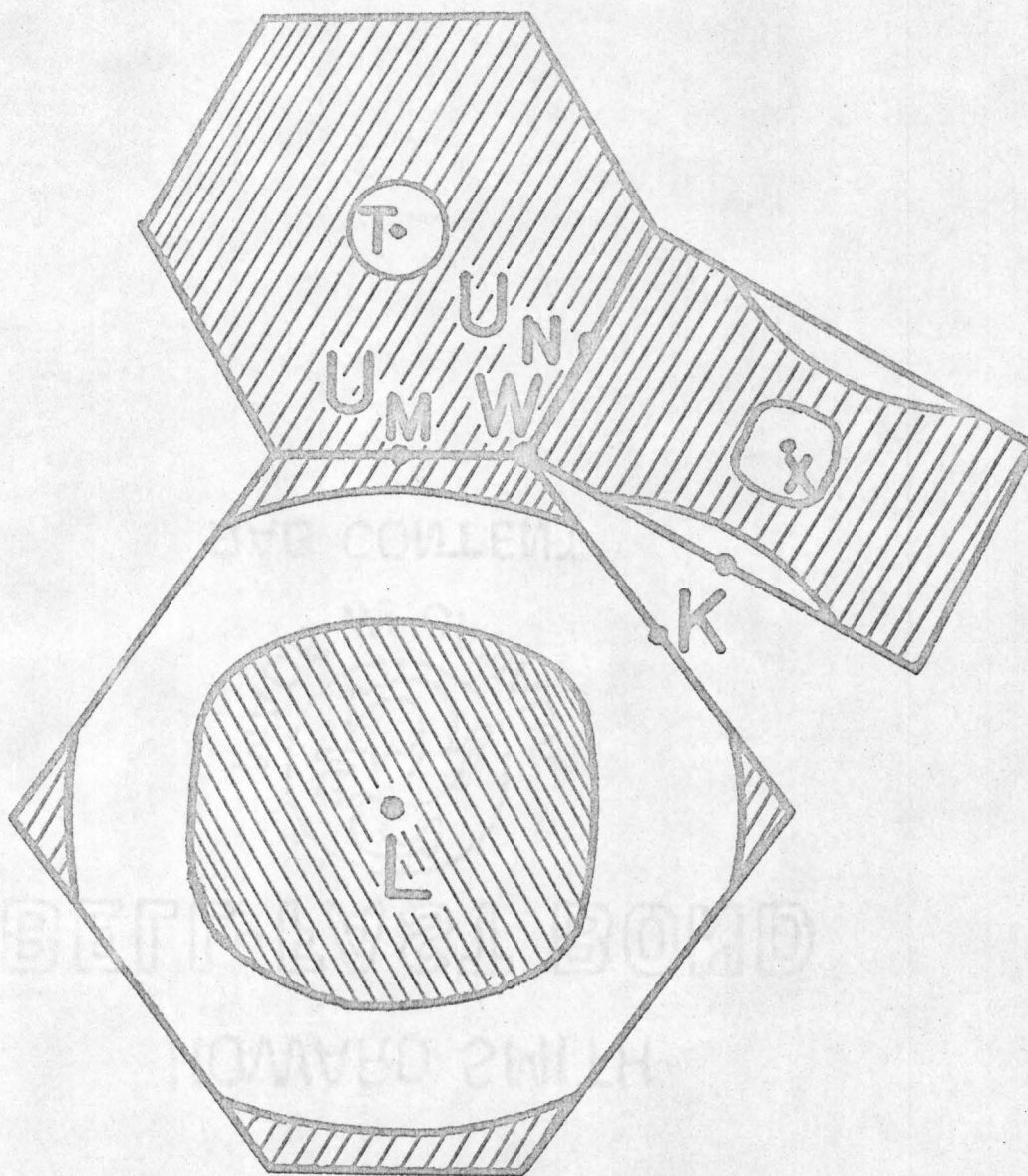


FIGURE 33

INTERSECTION OF THE FERMI SURFACE WITH THE  
BRILLOUIN ZONE FACES, RAPW APPROXIMATION

this orbit did not exist. The area of contact of the Fermi surface with the T-face of Figure 33 must be enlarged slightly to agree with the magnetoresistance data. In general, the calculation agrees reasonably well with the data of these experiments, and is a good approximation of the actual Fermi surface.

E. A Discussion of the Possible Effects of the Curved Sample Surface on the Cyclotron Resonance Signals

The subsidiary maxima on the low-field side of the cyclotron resonance derivative signals (see Figures 14 and 16) was attributed to the effects of a slightly-curved sample surface. The effects of small-angle tipping of the sample surface with respect to the DC magnetic field have been discussed by several investigators (e.g., Koch, Stradling, and Kip, 1964, Langenberg and Marcus, 1964, Grimes and Kip, 1963, Spong and Kip, 1965). One explanation for the effects of field-tipping, which included signal-splitting much like that observed from the curved sample surfaces in mercury, invoked the Doppler-shifted electromagnetic field seen by an electron slowly spiralling down out of the skin depth. Because of the curved sample surface of the mercury crystals, electrons from the same orbit on the Fermi surface would spiral up toward the sample surface, or down from it, depending upon their position in the sample. Because the electromagnetic field changes in phase as well as in amplitude as the electron spirals away from or toward the surface, one of these groups of electrons will resonate at  $H < H_c$ , the other at  $H > H_c$ . The effect of this mechanism on the derivative of a cyclotron

resonance signal is not clear because of the complicated shape of the signal itself (see Figure 3). One of the effects of a tilted sample surface reported by other investigators was the large phase shift of the resonance signals observed. The phase shifts observed in this experiment were small for most signals (of the order of  $n \leq \pm 0.05$  for the data of Figure 17). Another mechanism that has been suggested to explain the tipping effects involves the creation of sheets of current deep in the metal by the electrons spiralling down from the skin depth. Electrons spiralling up toward the skin depth then react with these current sheets, and upon arriving at the skin depth, modify the surface impedance in such a way as to cause peak-splitting, inversion, and possibly mass-doubling (Grimes and Kip, 1963). None of the explanations is completely satisfactory in explaining the results observed in mercury, but because the phase shift observed was small, especially for the data of Figures 17 and 21, the mass shift caused by the curved surface is expected to be small.

#### F. Conclusions

Cyclotron resonance signals with as many as twenty subharmonics have been observed in single-crystal mercury. Cyclotron mass results are reported from four samples having different crystal orientation. The minimum cyclotron effective mass of the electron lenses ( $\alpha$ -orbits) was found to be  $0.63 m_0$ , for a magnetic-field direction along the binary direction. An ellipsoidal fit to the cyclotron effective mass data from the electron lenses showed that they can be roughly approximated by an

ellipsoid of revolution, with the parameters  $m_1 = m_2 = 0.219 m_0$ ,  $m_3 = 1.84 m_0$ . The minimum cyclotron effective mass of the  $\gamma$ -orbit (see Figure 8) was found to be  $0.69 m_0$ , with the magnetic field directed along a bisectrix direction. A third set of masses, labelled E in Figure 21, do not have the proper anisotropy to match any part of the Fermi surface, and the origin of these masses cannot be explained. The minimum mass of this curve was  $0.16 m_0$ . Only one set of resonances was observed in the parallel-polarization position, corresponding to the  $\alpha$ -orbits.

The magnetoresistance experiment shows the usefulness of studying magnetoresistance in a compensated metal over a large angular range centered about the transverse magnetoresistance position. The magnetic-field dependence of the transverse magnetoresistance has confirmed that mercury is a compensated metal. The quadratic dependence of the magnetoresistance did not completely disappear even when the magnetic field was accurately aligned perpendicular to an open orbit direction. Two sets of open orbits were observed -- a band of primary periodic open orbits along the  $\{100\}$  reciprocal lattice directions, and a band of secondary periodic open orbits along the binary directions. The absence of the binary-directed orbit for a magnetic-field direction along the  $(100)$  direction is proof that the Fermi surface touches the T-faces of the Brillouin zone.

Quantum oscillations of the microwave surface impedance were observed at high magnetic-field strengths during the cyclotron resonance experiments. These oscillations had a frequency equal to  $1.12 \times 10^{-6}$

Gauss<sup>-1</sup> with the magnetic field along a bisectrix direction, and are attributed to the  $\beta$ -orbits.

A comparison of the results of these experiments has been made with Keeton and Loucks' model of the Fermi surface. In general it was found to be in good agreement with the experimental results; however, it does not explain the origin of the cyclotron masses labelled E in Figure 21.

BIBLIOGRAPHY

- Ashcroft, N. W., Phys. Rev. 140, A938 (1965).
- Azbel', M. Ya., J. Phys. Chem. Solids 7, 105 (1958).
- Azbel', M. Ya., and Kaner, E. A., Sov. Phys. J.E.T.P. 3, 772 (1956).
- Azbel', M. Ya., and Kaner, E. A., J. Phys. Chem. Solids 6, 113 (1958).
- Barrett, C. S., Acta. Cryst. 10, 58 (1957).
- Brandt, G. B., and Rayne, J. A., Physics Letters 15, 18 (1965).
- Brandt, G. B., and Rayne, J. A., to be published (1966).
- Chambers, R. G., Proc. Phys. Soc. 86, 305 (1965).
- Datars, W. R., and Dixon, A. E., Bull. Am. Phys. Soc. 11, 252 (1966).
- Datars, W. R., and Vanderkooy, J., I.B.M. Journal of Res. and Dev. 8, 247 (1964).
- Dexter, R. N., Zeiger, H. J., and Lax, B., Phys. Rev. 104, 637 (1956).
- Dishman, J. M., and Rayne, J. A., Physics Letters 20, 348 (1966).
- Dixon, A. E., and Datars, W. R., Solid State Comm. 3, 377 (1965).
- Dixon, A. E., and Datars, W. R., Bull. Am. Phys. Soc. 11, 252 (1966).
- Dresselhaus, G., Kip, A. F., and Kittel, C., Phys. Rev. 98, 368 (1955).
- Fawcett, E., Phys. Rev. 103, 1582 (1956).
- Fawcett, E., Advances in Physics 13, 139 (1964).

- Galt, J. K., Merritt, F. R., and Klauder, J. R., Phys. Rev. 139, A823 (1965).
- Grimes, C. C., and Kip, A. F., Phys. Rev. 132, 1991 (1963).
- Gustafson, D. R., Mackintosh, A. R., and Zaffarano, D. J., Phys. Rev. 130, 1455 (1963).
- Harrison, W. A., Phys. Rev. 118, 1190 (1960).
- Heine, V., Phys. Rev. 107, 431 (1957).
- Jones, H., The Theory of Brillouin Zones and Electronic States in Crystals (North Holland Publishing Co., Amsterdam, 1960), p. 58.
- Keeton, S. C., and Loucks, T. L., Phys. Rev. (to be published) (1966).
- Khaikin, M. S., Mina, R. T., and Edel'man, V. S., Sov. Phys. J.E.T.P. 16, 1459 (1963).
- Kip, A. F., Langenberg, D. N., and Moore, T. W., Phys. Rev. 124, 359 (1961).
- Kip, A. F., Langenberg, D. N., Rosenblum, B., and Wagoner, G., Phys. Rev. 108, 494 (1957).
- Koch, J. F., Stradling, R. A., and Kip, A. F., Phys. Rev. 133, A240 (1964).
- Langenberg, D. N., and Marcus, S. M., Phys. Rev. 136, A1383 (1964).
- Lifshitz, I. M., Azbel', M. Ya., and Kaganov, M. I., Sov. Phys. J.E.T.P. 4, 41 (1957).
- Loucks, T. L., Phys. Rev. 139, A1333 (1965).
- Mattis, D. C., and Dresselhaus, G., Phys. Rev. 111, 403 (1958).

Pippard, A. B., Proc. Roy. Soc. A191, 385 (1947).

Pippard, A. B., Low Temperature Physics (edited by DeWitt, C., Drefuss, B., and deGennes, P. G., Gordon and Breach, New York, 1962), p. 131.

Shaw, M. P., Eck, T. G., and Zych, D. A., Phys. Rev. 142, 406 (1966).

Shaw, M. P., Sampath, P. I., and Eck, T. G., Phys. Rev. 142, 399 (1966).

Shockley, W., Phys. Rev. 90, 491 (1953).

Shoenberg, D., Phil. Trans. A245, 1 (1952).

Spong, F. W., and Kip, A. F., Phys. Rev. 137, A431 (1965).

Verkin, B. I., Lazarev, B. G., and Rudenko, N. S., Doklady Akad. Nauk. S.S.S.R. 80, 45 (1951).

Ziman, J. M., Electrons and Phonons (Oxford University Press, London, 1960), p. 374.